Science
AAAS

Supplementary Materials for

A solution-processed radiative cooling glass

Xinpeng Zhao *et al*.

Corresponding author: Liangbing Hu, binghu@umd.edu

Science **382**, 684 (2023)
DOI: 10.1126/science.adi2224

The PDF file includes:

Materials and Methods

Materials

Low-melting-point glass microparticles (P_2O_5-Al_2O_3-Na_2O-K_2O-B_2O_3-SiO_2) with a particle diameter of 2–15 μm (average particle size of 6.3 μm), a density of 2.56 g/cm^3, and a softening temperature of ~350 °C and high-purity α-Al_2O_3 particles (99.99%) of ~0.3–1.0 μm in size (average ~0.5 μm) were used for fabrication. Ethanol (> 97%) was used to prepare the slurry for coating. The square ceramic floor and wall (quarry) tiles with a size of 15 cm × 15 cm and transparent float glass with a size of 5 cm × 5 cm were used for substrates. Iron (III) oxide (Fe_2O_3, particle size <5 μm, purity ≥ 99 %), montmorillonite K10 powder (surface area is 220 to 270 m^2/g), nanoclay (hydrophilic bentonite, particle size ≤ 25 μm), sodium chloride (NaCl), sodium nitrate ($NaNO_3$), calcium sulfate dihydrate ($CaSO_4 \cdot 2H_2O$), humid acid, and carbon black (2–12 μm, 99.95%) were used for resistance test. All materials were used as supplied without additional purification.

Fabrication of the white radiative cooling glass coating

The raw materials including low-melting-point glass particles and Al_2O_3 particles were mixed at different mass ratios (e.g., 1:1). The mixed particles were then dispersed in ethanol at a concentration of 0.75 g/ml to prepare a uniform slurry for brush painting, air spray coating, or blade coating. After applying the slurry at a thickness of ~550 μm on the ceramic tile, the coating was air-dried in a fume hood for ~3 min to completely evaporate the ethanol. Subsequently, the dried coating was heated at 600 °C for <1 min in a muffle furnace (FB1315M, Thermo Fisher Scientific, heating rate is ~40 °C/min). Note that the slurry did not include any binders, resulting in a maximum achievable coating thickness of ~350 μm, beyond which cracks are likely to form. Within each cycle, the deposition thickness is modifiable, ranging from 50 to 350 μm, depending on both the slurry concentration and the applied volume. For a 50 wt.% Al_2O_3, two coating cycles are required to reach a solar reflectance of > 0.95 at a 500 μm thickness, whereas a single brush coating achieves the same reflectance at roughly 300 μm thickness for 60 wt.% or 70 wt.% Al_2O_3.

Fabrication of the colored radiative cooling glass coating

The phosphor (e.g., nitride ($CaAlSiN_3$:Eu^{2+}), $(Sr,Ba)_2SiO_4$:Eu^{2+}, and (Ce,Gd):YAG) with a mass ratio of 10 wt.% was first added to the mixture of the white radiative cooling glass (50 wt.% glass particles and 50 wt.% Al_2O_3) to prepare the raw materials. The mixed particles (i.e., glass, Al_2O_3, and phosphor) were then dispersed in ethanol at a concentration of 0.75 g/ml to prepare a uniform slurry for the coating. The colored slurry was then coated on the ceramic tile with a thickness of ~550 μm and dried in a fume hood for ~3 min. The colored radiative cooling glass coating was then obtained by heating at 600 °C for ~1 min in a muffle furnace (FB1315M, Thermo Fisher Scientific).

Fabrication of the radiative cooling glass coating with a dense transparent protective layer

The slurry consisting of glass particles and Al_2O_3 particles was first applied at a thickness of ~550 μm on the ceramic tile following the same process for fabricating the white radiative cooling glass coating. Subsequently, another layer of pure low-melting-point glass particles uniformly dispersed in ethanol (0.75 g/ml) was added to the top of the deposited 550-μm-thick layer at a thickness of ~10 μm. After air drying, the bilayer coating was obtained by heating at 600 °C for ~1 min in a muffle furnace (FB1315M, Thermo Fisher Scientific).

Process of filling resin to the porous radiative cooling glass

To fill the porous radiative cooling glass with epoxy resin, the two liquid components of the resin were mixed at a ratio of 2 to 1. Then, the porous radiative cooling glass coating was placed at the bottom of a mold and immersed in liquid resin. To remove any gas and ethanol solvent in the porous glass coating, the solution was degassed under 200 Pa. After approximately 5 minutes, the vacuum was released to let the resin fill into the porous radiative cooling glass coating by atmospheric pressure. This process was repeated three times to ensure complete infiltration of the resin into the porous glass coating. Finally, the mold containing the porous radiative cooling glass coating and resin was kept static at 30 °C for 12 hours.

Materials characterization

The solar reflectance (0.3–2.5 μm) of the materials was measured using an ultraviolet (UV)-vis-near-IR spectrophotometer (Shimadzu UV-3600i Plus) with an integrating sphere (ISR-1503, diameter of 150 mm). Note that we assumed a solar reflectance value of 0.99 for the wavelength range of 1.3-2.5 μm since our measured values exceeded 1.0. A Fourier transform infrared spectrometer (Thermo Nicolet NEXUS 670 FTIR) with a gold-coated integrating sphere was used to measure the absorption/emissivity of the glass-ceramic coating in the wavelength range of 4–20 μm. A scanning electron microscope (SEM; Tescan XEIA) was used to characterize the morphology and structure of the pigments and ceramic coatings and obtain elemental maps by performing energy dispersive spectroscopy (EDS). X-ray scattering (Rigaku Ultima III; 40 kV, 30 mA, Cu Kα, $\lambda = 1.5406$ Å) was used to characterize the crystal polymorphism of the pigments and coatings. The high-temperature flame shock was performed using a butane gas flame torch, with a flow rate of 100 g/hr. The infrared temperature mapping was performed by an infrared camera VarioCAM HDx head 600 (7.5–14 μm) with a resolution of 640×480 infrared pixels using a standard lens (20 mm). The particle/pore size distributions were derived from SEM images using ImageJ software, with particle sizes determined by the maximum Feret diameter. To ensure representative results, over 30 particles from various regions within the SEM images were analyzed. Micro-computed tomography (Micro-CT, SkyScan 1272, Micro Photonics, Inc.) was conducted to validate the pore size distribution and porosity of the radiative cooling glass coating determined using SEM and ImageJ software. The dynamic test, simulating raindrop impact via jet impingement, was conducted using a pipe with a diameter of 0.5 cm. Throughout the test, the pipe was positioned around 40 cm above the coating, and water was released at an outlet flow rate of approximately 20 mL/s to impact the coating continuously for 24 hours.

Adhesion resistance test

We evaluated the adhesion strength of the radiative cooling glass coating following ASTM Standard D3359-22 (*52*). To meet Test Method A, the radiative cooling glass coating applied on the ceramic tile was prepared for the test at a thickness of approximately 100 μm. A multi-blade cutter with a tooth spacing of 2 mm was kept vertical to the plane of the tested sample and used to cut the radiative cooling glass coating at a speed of 30 mm/s. Then, the sample was rotated 90° and the same cutting process was repeated to form a grid lattice graphic. After the required cuts, a soft brush was used to remove the detached flakes. Subsequently, a tape (600-1PK, 3M) was placed on the grid with good and even contact between the adhesive of the tape and the coated surface. After 90 s, the tape was removed by grasping the free end and quickly backing away from it at an angle as close to 180°.

Hardness test

We conducted the standard pencil test for measuring the hardness of the radiative cooling glass coating following ASTM D3363-22 (*53*). In a typical test, sharpened pencils of increasing hardness levels are held at a 45° angle and pushed over 1 cm on the specimen's surface in a single stroke. The coating's resistance to the pencil's scratch measures its hardness. The test continues until a pencil is found that ruptures the coating, and the hardest pencil that does not cause rupture is recorded as the hardness level of the coating. The weight applied during this process can vary; in our study, we used weights of 500 g and 1000 g.

UV-radiation aging test and water resistance test

We performed UV aging tests in a home-built chamber to investigate the degradation of the white radiative cooling glass coatings. UV radiation with a power density of ~5.0 W/m^2 was provided by a UVB T5 lamp, which provides peak radiation with a wavelength of ~305 nm. The samples were subjected to UV irradiation for 80 days, which is equivalent to 3 years of sun exposure in Florida (annual UV dose of ~280 MJ/m^2)(*49*, *50*). The temperature and relative humidity were 21 °C and 50%, respectively. The water resistance of the white radiative cooling glass coating was evaluated by completely immersing the samples in water for 60 days.

Soiling resistance test

We evaluated the soiling resistance of the developed glass coatings following ASTM D7897-18 (*51*). Four soiling agents, including mineral dust, inorganic salts, humic acids, and carbon black, which are similar to atmospheric particles (e.g., dust, salts, particulate organic matter (POM, and soot), were prepared to mimic the natural soiling process. Fe_2O_3 (0.3 ± 0.02 g, particle size < 5 μm, purity ≥ 99 %), montmorillonite K10 powder (1.0 ± 0.05 g, surface area: 220 to 270 m^2/g), and nanoclay (1.0 ± 0.05 g, hydrophilic bentonite, particle size ≤ 25 μm) were dispersed into 1.0 L of distilled water to prepare the mineral dust suspension of 2.3 ± 0.1 g/L. Sodium chloride (NaCl, 0.3 ± 0.03 g), sodium nitrate ($NaNO_3$, 0.3 ± 0.03 g), and calcium sulfate dihydrate ($CaSO_4 \cdot 2H_2O$, 0.4±0.03 g) were dissolved into 1.0 L distilled water to prepare the inorganic salt solution with an overall concentration of 1.0 ± 0.1 g/L. Humid acid (1.4 ± 0.05 g) was dissolved into 1.0 L of distilled water to prepare the solution of POM. Carbon black (1.37±0.05 g) was dispersed into 1.0 L of distilled water and shaken for five minutes to prepare a stable soot suspension. Considering the natural soiling in various climates is different, three different mixtures of the above four soiling agents (i.e., mineral dust, inorganic salts, humic acid, and carbon black) were prepared to simulate the three typical climates that may be suitable for the application of the radiative cooling material, namely, hot and dry (e.g., Phoenix, Arizona), hot and humid (e.g., Miami, Florida), and moderate (i.e., hot summer and cold winter, e.g., Youngstown, Ohio). Details can be found in Table S1. The soiling mixture was deposited on the surface of the coatings with a wet soiling mass of 0.8 ± 0.1 g/m^2 using an air spray gun (PointZero, 0.3 mm stainless steel needle, 10 psi air pressure).

Table S1. Composition of soiling mixture for various climates.

	Dusts	Salts	POMs	Soots
Hot and Dry	79%	20%	0%	1%
Hot and humid	16%	7%	69%	8%
Moderate	61%	31%	0%	8%

Supplementary Text

Table S2. Preliminary cost analysis for the radiative cooling glass coatings.

Materials	Purchase link	Price ($/ton)	Dosage (kg/m^2)	Cost ($/m^2)
Low melting point glass powders	https://www.alibaba.com/product-detail/Low-melting-point-glass-ceramic ceramic_1600712212701.html	160	~0.8	0.128
High purity 99.9% Al_2O_3 particles	https://www.alibaba.com/product-detail/Aluminium-Oxide-Nanoparticles-High-Purity-99_1600226288435.html?s=p	700	~0.8	0.560
Total				0.688

Table S3. Comparison of this work with state-of-the-art daytime radiative cooling structures.

		S. Fan, 2014, *Nature* (*15*)	**X. Yin and R. Yang, 2017, *Science* (*19*)**	**Y. Yang, 2018, *Science* (*21*)**	**B. Huang, 2022, *Adv. Mater.* (*29*)**	**D. Wan, 2023, Nano today (*54*)**	**This work**
Design	**Structure**	Multi-layer thin films	Polymer-silver bilayer	Porous-polymer	Multi-layer thin coatings	Silica nanofibers network	Porous glass/Al_2O_3
	Binders	NA	NA	Polymer	Silver	NA	Glass
	Ink/slurry-based	No	No	Yes	Yes	No	Yes
Performance	**Solar reflectance**	0.97	~ 0.96	0.97 ± 0.02	~ 0.964	0.97	> 0.96
	Emissivity	0.7	0.93	0.96 ± 0.03	0.946	~0.90	0.95
	Operating temperature	< 300 ºC	< 150 ºC	< 150 ºC	< 300 ºC	Over 1200 ºC	Up to 1000 ºC
	Color	No	No	Yes	No	No	Yes
	Durability	No	No	No	No	No	Yes
Fabrication & Cost	**Processes**	Vacuum deposition	Polymer extrusion +Vacuum deposition	Brush coating	Spray coating+Langmuir–Schaefer (LS) self-assembly	Electrospinning (slow)	Spray/brush coating (fast)
	Cost	Very high	Medium	Low	High	High	Low

Theoretical modeling of the scattering and absorption properties of the glass and Al_2O_3 particles

The Lorenz-Mie theory was used to describe the optical properties of a single particle, which states (*55, 56*),

$$Q_{\text{sca}} = \frac{2}{x^2}\sum_{n=1}^{\infty}(2n+1)(|a_n|^2 + |b_n|^2) \quad \text{(S1)}$$

$$Q_{\text{ext}} = \frac{2}{x^2}\sum_{n=1}^{\infty}(2n+1)\text{Re}(a_n + b_n) \quad \text{(S2)}$$

$$Q_{\text{abs}} = Q_{ext} - Q_{sca} \quad \text{(S3)}$$

where Q_{ext}, Q_{sca}, and Q_{abs} are the extinction efficiency, scattering efficiency, and absorption efficiency of the particle, respectively, $x = kD/2$ is the size parameter, D is the diameter of the particle, $k = 2\pi/\lambda$ is the wave number, λ is the wavelength of the incident radiation, Re[·] corresponds to the real part of a complex quantity, and a_n and b_n are the Mie coefficients which

are a function of particle size, the wavelength of the incident radiation, and the complex refractive index of the simulated particle.

Averaging of solar reflectance and infrared emissivity in transparency atmospheric window

The spectrally-averaged solar reflectance, γ, can be evaluated using the spectral solar radiation intensity of air mass 1.5 ($I_{sol,\lambda}$, AM1.5) as a weighting factor, as given by,

$$\gamma = \frac{\int_{0.3\ \mu m}^{2.5\ \mu m} \gamma_\lambda I_{sol,\lambda} d\lambda}{\int_{0.3\ \mu m}^{2.5\ \mu m} I_{sol,\lambda} d\lambda} \tag{S4}$$

where γ_λ is spectral reflectance in solar region. The spectrally-averaged absorption efficiency, α, can be evaluated using the spectral blackbody emissive power in the 8–13 μm range as a weighting factor. This is given by,

$$\alpha = \frac{\int_{8\ \mu m}^{13\ \mu m} \alpha_\lambda I_{b\lambda} d\lambda}{\int_{8\ \mu m}^{13\ \mu m} I_{b\lambda} d\lambda} \tag{S5}$$

where, $I_{b\lambda} = \frac{2hc_0^2}{\lambda^5[exp(hc_0/\lambda k_b T)-1]}$, $h = 6.626 \times 10^{-34}$ J·s is the universal Plank constant, $k_b = 1.381 \times 10^{-23}$J/K is the Boltzmann constant, and $c_0 = 2.998 \times 10^8$ m/s is the speed of light in vacuum.

Simulation of the reflectance and absorption of randomly distributed Al_2O_3 and SiO_2 particles

We implemented numerical simulations to model the reflectance and absorption of randomly distributed Al_2O_3 and SiO_2 particles within a high-volume fraction, leveraging the Maxwell equations,

$$\mu_0 \varepsilon_0 \frac{\partial^2 \mathbf{E}}{\partial t^2} - \nabla^2 \mathbf{E} = 0, \tag{S6}$$

$$\mu_0 \varepsilon_0 \frac{\partial^2 \mathbf{B}}{\partial t^2} - \nabla^2 \mathbf{B} = 0. \tag{S7}$$

where **E** is the electric field, **B** is the magnetic field, and μ_0 and ε_0 are the permittivity and permeability of free space, respectively. Our simulations utilized a high-speed Finite-Difference Time-Domain (FDTD) solver (Tidy3D) (*42*). The simulated region encompassed a three-dimensional (3D) rectangle with dimensions of 10 μm in length and width and a height of 100 μm. We dispersed the simulated particles (SiO_2 or Al_2O_3) randomly across the simulation area. The simulated wavelengths ranged from 0.3 to 2.5 μm for solar reflectance and from 4 to 20 μm for infrared emissivity. We ensured the plane wave was incident from the *z* direction while setting *x* and *y* as periodic boundary conditions. We used the perfectly matched layer (PML) as the boundary condition for the *z* direction. From the flow monitor, we obtained the reflection (*R*) and transmission (*T*) spectra, which we then normalized to the incident light. We calculated the absorption spectrum (*A*) from 1-*R*-*T*.

Theoretical modeling of radiative cooling performance

The net cooling power, $P_{net}(T)$, of a surface exposed to solar radiation and clear sky can be

expressed as (*15*),

$$P_{net}(T) = (1 - R_{solar})P_{sun} + P_{conv+cond}(T, T_{amb}) + P_{atm}(T_{amb}) - P_{rad}(T) \quad \text{(S8)}$$

where T represents the surface temperature and T_{amb} is the ambient temperature (i.e., air temperature near the ground), and R_{solar} denotes the average solar reflectance of the surface,

$$R_{solar} = \frac{\int_0^{\pi/2} \int_{0.3\ \mu m}^{2.5\ \mu m} R(\lambda, \theta) cos\theta I_{AM,1.5}(\lambda) d\lambda\, d\theta}{\int_{0.3\ \mu m}^{2.5\ \mu m} I_{AM,1.5}(\lambda) d\lambda} \quad \text{(S9)}$$

where $R(\lambda, \theta) = 1.0 - \epsilon(\lambda, \theta)$ signifies the spectral solar reflectance (0.3–2.5 μm), θ is the angle between the incident solar radiation and the normal direction of the emitted surface (*i.e.*, zenith angle), $\epsilon(\lambda, \theta)$ represents the surface emissivity of the panel as a function of wavelength and directional angle, and $I_{AM,1.5}(\lambda)$ refers to the air mass 1.5 (AM 1.5) solar spectrum. P_{sun} is the power density of the solar irradiance reaching the panel surface, which can be calculated as,

$$P_{sun} = \int_0^{\infty} I_{solar}(\lambda) d\lambda \quad \text{(S10)}$$

where $I_{solar}(\lambda)$ denotes the spectral solar radiation, including both direct and diffusive components. $P_{conv+cond}$ represents the surface's heat gain received from the surroundings through conduction and convection, which can be calculated as follows (*57*),

$$P_{conv+cond} = h(T_{amb} - T) \quad \text{(S11)}$$

where $h = 8.3 + 2.5v$ represents the overall heat transfer coefficient between the panel surface and the surroundings, measured in the unit of W/(m^2·K), with v representing the wind speed (m/s). P_{atm} denotes the radiative heating received from atmospheric thermal radiation, which can be expressed by,

$$P_{atm} = \int d\Omega \cos\theta \int_0^{\infty} \epsilon(\lambda, \theta) \epsilon_{atm}(\lambda, \theta, PW) I_b(\lambda, T_{amb}) d\lambda \quad \text{(S12)}$$

where Ω represents the solid angle of a hemisphere, with $\int d\Omega = 2\pi \int_0^{\pi/2} d\theta sin\theta$, ϵ_{atm} is the emissivity of the atmosphere as a function of the directional angle of the coating surface, wavelength, and atmospheric precipitable water (PW), $I_{b\lambda}$ is the spectral intensity of the blackbody radiation. The precipitable water is quantified as the thickness that atmospheric water vapor would assume upon condensation into liquid, and this can be approximated using the equation (*58*),

$$PW \approx 2.15RH \frac{3800exp\left(\frac{17.63T_{amb}}{T_{amb} + 234.04}\right)}{p_{atm}} - 0.82 \quad \text{(S13)}$$

where p_{atm} is the ambient pressure (Pa). We used the software MODTRAN (*59*) to obtain the atmospheric spectral emissivity that can be computed as a function of the precipitable water. The emissivity of the atmosphere can be approximated as follows,

$$\epsilon_{atm}(\lambda,\theta) = 1 - \left(1 - \epsilon_{atm}(\lambda,0)\right)^{1/cos\theta} \quad \text{(S14)}$$

where $\epsilon_{atm}(\lambda,0)$ denotes the atmospheric emissivity when the zenith angle is 0. Q_{rad} represents the radiative heat that spans all possible wavelengths and directions from the panel to the sky, and can be calculated as,

$$Q_{rad} = \int d\Omega \cos\theta \int_0^{\infty} \epsilon(\lambda,\theta) I_{b\lambda}(T) d\lambda \quad \text{(S15)}$$

Note that the surface emissivity $\epsilon(\lambda,\theta)$ in Eq.(S12) is assumed to be temperature-independent.

Modeling of the energy consumption, cost, and CO_2 emission of a reference midrise apartment building

We used EnergyPlus (version 22.2) to calculate the energy consumption, utility costs, and CO_2 emissions of a reference building with radiative cooling glass coating applied on the roof. The energy models are governed by energy-balance equations that consider climate, heat transfer through internal and external building enclosures, as well as heat sources and sinks, such as lighting, equipment (e.g., refrigerator, laundry appliances), and occupants. Both direct fluxes, as well as influxes reflected from the surroundings and ground, are included for evaluating radiative heat exchange with the ambient. The energy consumption of the simulated building was first derived by solving the governing equations iteratively over a year with a time step of 10 min. The utility cost calculations were based on the electricity and natural gas prices in 2020 from the U.S. Energy Information Administration (EIA) (*60, 61*). The CO_2 emissions were obtained by using the emission factors of electricity generation and natural gas combustion from the U.S. Environmental Protection Agency (EPA) (*62*) and the U.S. Department of Energy (DOE) (*63*). To extend our results to the entire country, we selected sixteen cities that cover all climate zones in the United States, including Albuquerque (NM), Atlanta (GA), Austin (TX), Boulder (CO), Chicago (IL), Duluth (MN), Fairbanks (AK), Helena (MT), Honolulu (HI), Las Vegas (NV), Los Angeles (CA), Minneapolis (MN), New York City (NY), Phoenix (AZ), San Francisco (CA), and Seattle (WA). We used the reference midrise apartment provided by the U.S. Department of Energy as our building model (*64*). Both old structures built prior to 1980 (pre-1980) and new ones built after 2004 (post-2004) were studied. The modeled midrise apartment reference building has a rectangular shape with 4 floors. The total floor area is 3135 m^2. The roof area is 783 m^2. The total external wall surface area is 1542 m^2. The windows cover 20% of the total wall surface area. We treated the DOE reference midrise apartment as the baseline model, then modified roof materials based on the properties of the radiative cooling glass coating to determine the energy savings, cost savings, and CO_2 emission reductions.

Table S4. Optical properties of standard roof and wall surfaces and the developed radiative cooling glass coating.

	Roof (ASHRAE standard 90.1(*65*))	Wall (ASHRAE standard 90.1(*65*))	Radiative cooling glass coating
Thermal absorptance (2.5–20 μm)	0.91	0.90	0.86
Solar reflectance/absorptance (0.3–2.5 μm)	0.30/0.70	0.22/0.78	0.96/0.04
Visible reflectance/absorptance (0.37–0.78 μm)	0.30/0.70	0.22/0.78	0.96/0.04

Simulation of the protective transparent glass layer on the radiative cooling glass coating

For simplification, we modeled the radiative cooling glass coating to have a thickness of 0.5 μm as an effective bulk medium with a refractive index of -5.7+0.3i. The thickness of the protective transparent glass layer ranged from 0–20 μm. We derived reflectance values by solving Maxwell's equations using the high-speed FDTD solver, Tidy3D (*42*). In our 2D simulations, we set the *x*-axis with periodic boundary conditions and the *y*-axis with a perfectly matched layer (PML) boundary condition, where a plane wave (e.g., incident light) was incident from the *y*-axis. We obtained the reflectance of the simulated structure from the flow monitor, then Fourier transformed and normalized to the incident light.

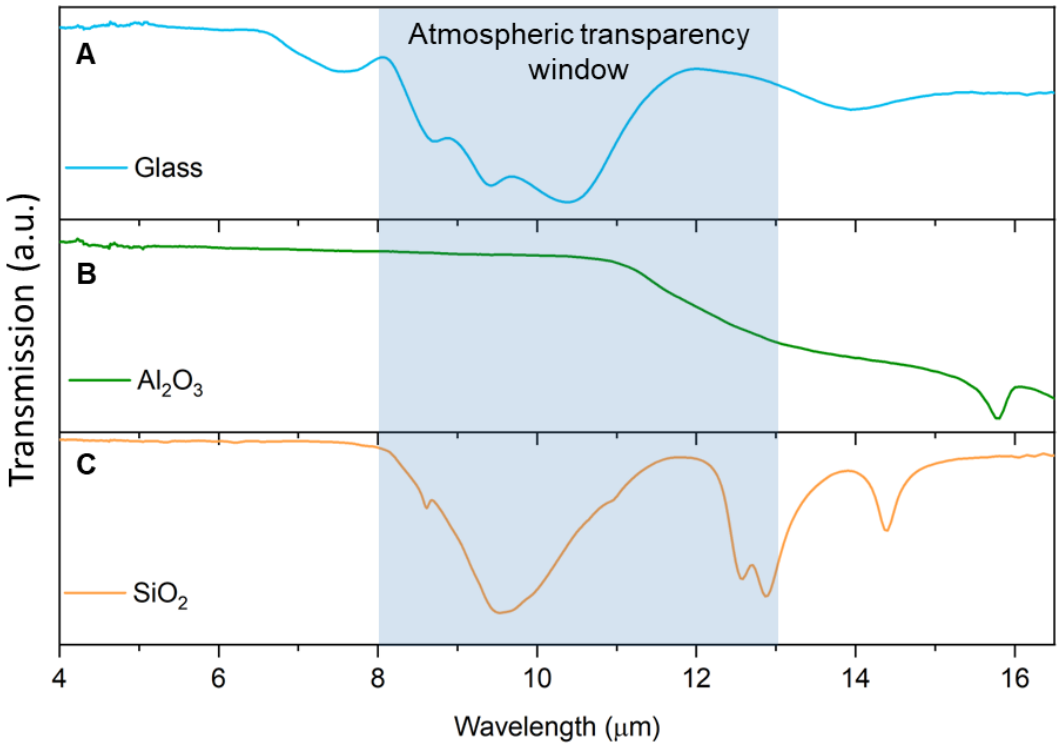

Figure S1. Fourier-transform infrared spectroscopy (FTIR) of the (**A**) glass particles, (**B**) Al_2O_3 particles, and (**C**) SiO_2 particles. The low-melting-point glass has rich absorption peaks in the 8–13 μm range, indicating selective emission in the atmospheric transparency window. The Al_2O_3 also shows increased absorption at wavelengths > 11 μm. Since the FTIR signals of glass and SiO_2 are similar (both have rich absorption peaks in the 8–13 μm range) and the complex refractive index of the low-melting-point glass in the 2.5–20 μm range is unknown, we used the complex refractive index of SiO_2 as input for Lorenz-Mie theory in our size optimization calculations.

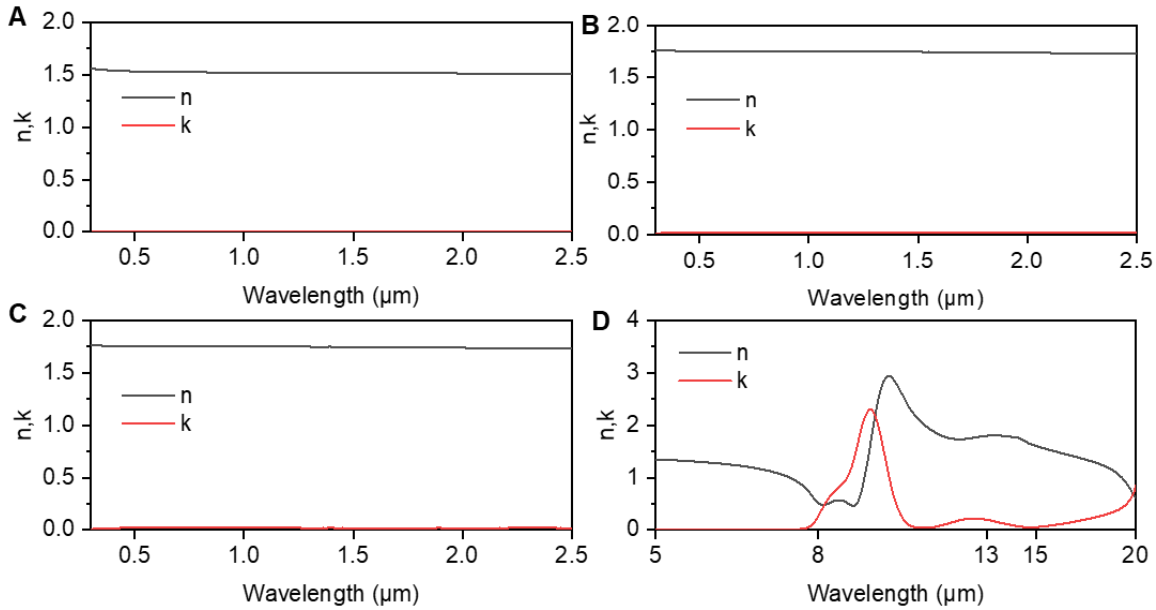

Figure S2. Complex refractive index of the (**A**) glass particles (*66*) and (**B**) Al_2O_3 particles (*67*) in the solar region (0.3–2.5 μm). Both the glass particles (a eutectic mixture of different dielectric oxides, including P_2O_5, SiO_2, Al_2O_3, Na_2O K_2O, and B_2O_3) and Al_2O_3 feature a high refractive index and very low extinction coefficient in the solar region. The complex refractive index of (**C**) Al_2O_3 (*67*) and (**D**) glass (i.e., SiO_2 (*68*)) particles in the range of 5–20 μm. The refractive index of a medium is expressed as a complex number $m(\lambda) = n(\lambda) + ik(\lambda)$, where $n(\lambda)$ is the real part and $k(\lambda)$ is the imaginary part. The former is the ratio of free-space light speed to the medium's phase speed, and the latter relates to absorption. Scattering is the only process possible with a real refractive index, while a complex index allows for both scattering and absorption (*69*).

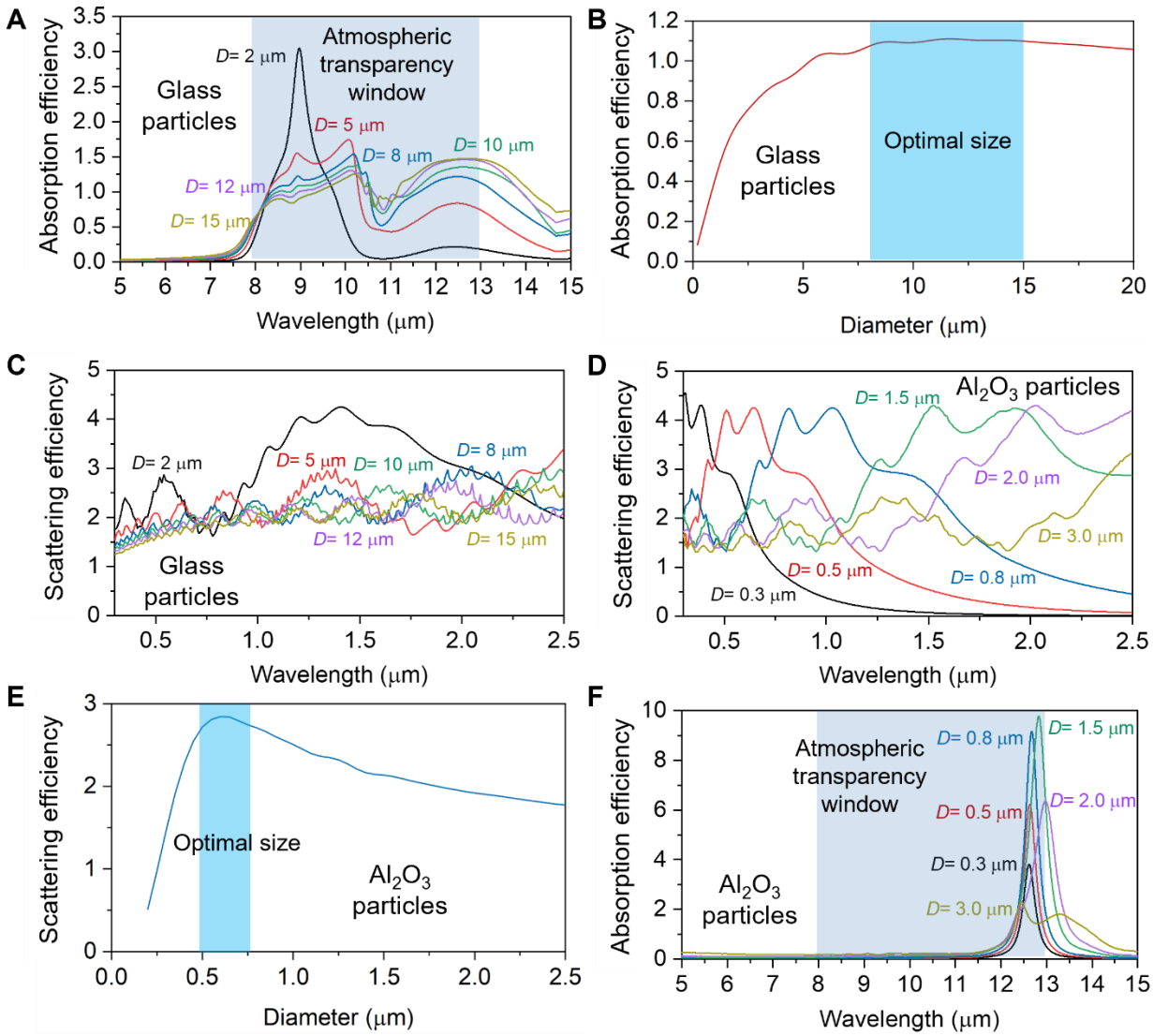

Figure S3. The calculated absorption and scattering efficiencies of the glass and Al_2O_3 particles as a function of wavelength and diameter based on Lorenz-Mie theory (Eqs. S1-S3). The complex refractive indices required for Lorenz-Mie theory calculations are obtained from Fig. S2. (**A**) The calculated absorption efficiency of glass particles (2–15 μm in diameter) in the wavelength range of 5–15 μm. The atmospheric transparency window (8– 13 μm) is shown in the shaded blue region. (**B**) Average absorption efficiency in the atmospheric transparency window of the glass particles as a function of diameter. The particles with diameters of 8–15 μm (blue region) result in maximum emissivity. (**C**) The calculated scattering efficiency of the glass particles (2–15 μm in diameter) in the wavelength range 0.3–2.5 μm. (**D**) The calculated scattering efficiency of the Al_2O_3 particles (0.3-3.0 μm in diameter) in the wavelength range of 0.3–2.5 μm. (**E**) Average scattering efficiency in the solar spectrum of Al_2O_3 particles as a function of diameter. Particles with diameters of 0.5–0.7 μm (blue region) result in maximum scattering efficiency. (**F**) The calculated absorption efficiency of Al_2O_3 particles (0.3-3.0 μm) in the wavelength range of 5–15 μm. The atmospheric transparency window (8– 13 μm) is shown in the shaded blue region.

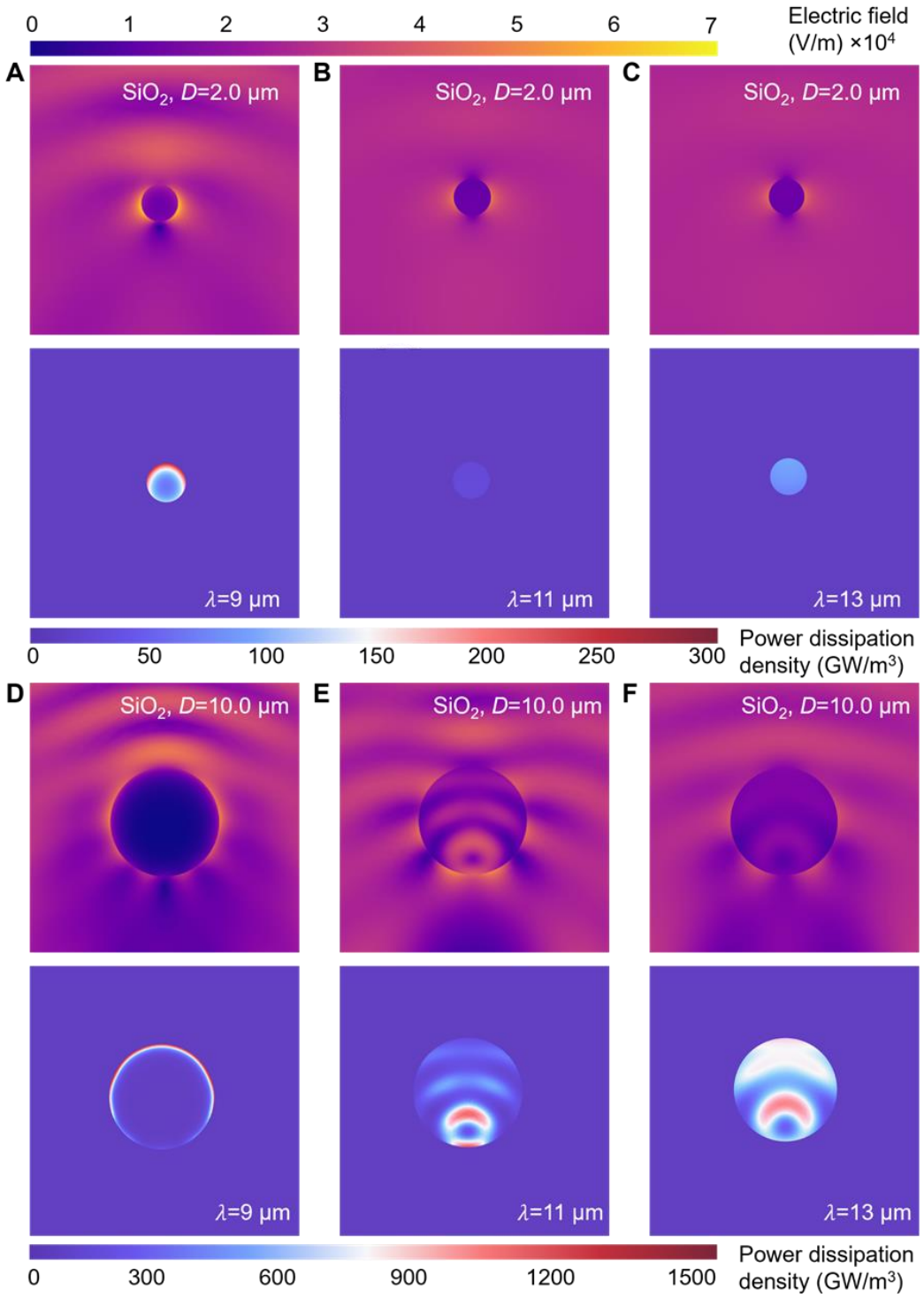

Figure S4. Simulated light scattering and absorption of SiO_2 particles with various diameters under different incident wavelengths in an air environment. (**A**) 2.0 μm diameter at 9.0 μm wavelength, (**B**) 2.0 μm diameter at 11.0 μm wavelength, (**C**) 2.0 μm diameter at 13.0 μm wavelength, (**D**) 10.0 μm diameter at 9.0 μm wavelength, (**E**) 10.0 μm diameter at 11.0 μm wavelength, (**F**) 10.0 μm diameter at 13.0 μm wavelength. The electric field intensity of the incident light is 1 V/m. For smaller SiO_2 particles (i.e., 2 μm, as shown in Figs. S4A-4C), the

resonance is predominantly electric-dipolar. The pronounced absorption peak around 9 μm is attributable to strong Fröhlich resonance at its phonon-polariton frequency of 9.7 μm, as corroborated by Fig. S2D. Beyond this frequency, absorption for the 2-μm-diameter SiO_2 particles declines rapidly. Conversely, when the SiO_2 particle size is 10 μm—close to the incident light wavelength—we observe the strong excitation of high-order Fröhlich resonances (Figs. S4D-4F), both electric and magnetic modes, which contribute to broadband emissivity across the entire atmospheric window.

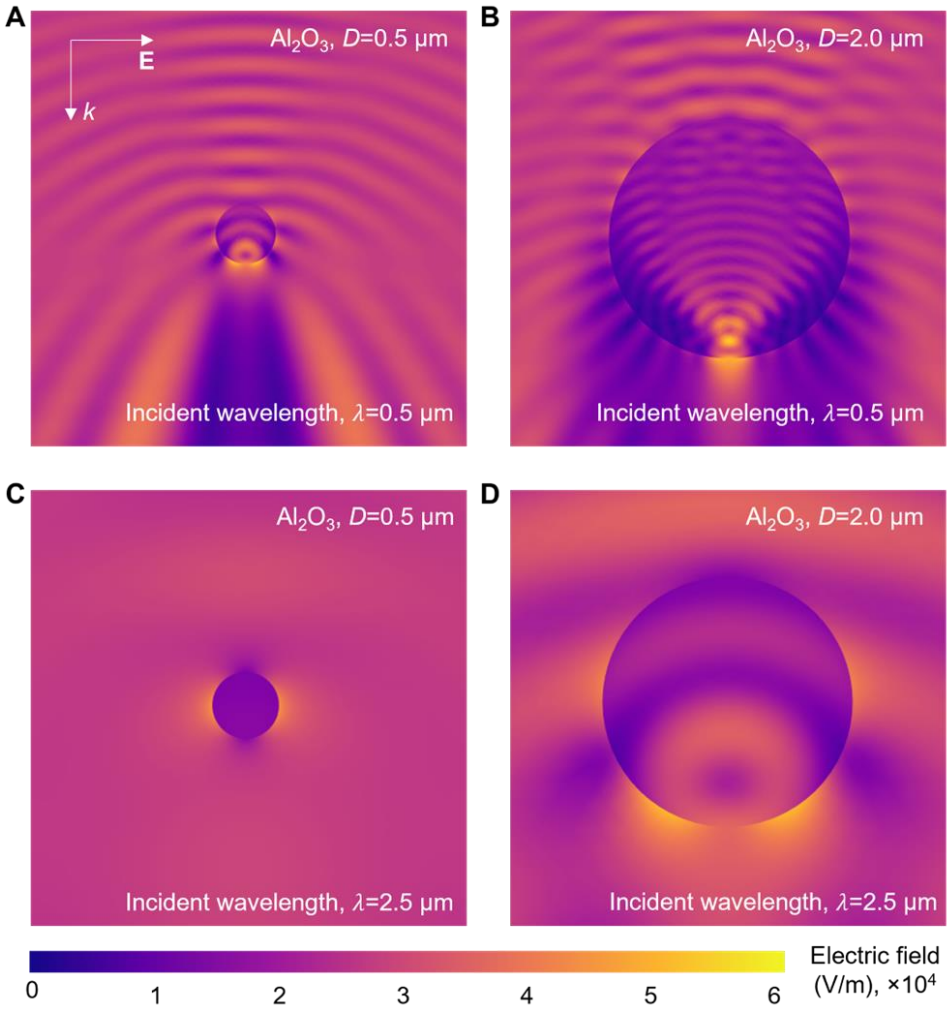

Figure S5. Simulated light scattering of Al_2O_3 particles with various diameters under different incident wavelengths in an air environment. (**A**) 0.5 μm diameter at 0.5 μm wavelength, (**B**) 0.5 μm diameter at 2.5 μm wavelength, (**C**) 2.0 μm diameter at 0.5 μm wavelength, (**D**) 2.0 μm diameter at 2.5 μm wavelength. The electric field intensity of the incident light is 1 V/m. Notably, forward scattering is prominent when the size of the Al_2O_3 particles is comparable to the wavelength of the incident light (Fig. S5A and Fig. S5D); this is a regime where Mie scattering is highly effective. Conversely, when the Al_2O_3 particles are substantially smaller than the incident wavelength (Fig. S5C), the size of the resonant cavity falls below the optical distance for one complete round trip of light, precluding the excitation of any significant resonance and consequently resulting in weak scattering. If the particle size surpasses the incident wavelength, the resonance wavelength shifts away from the incident wavelength, and numerous higher-order resonances are triggered, leading to enhanced scattering efficiency (Fig. S5D).

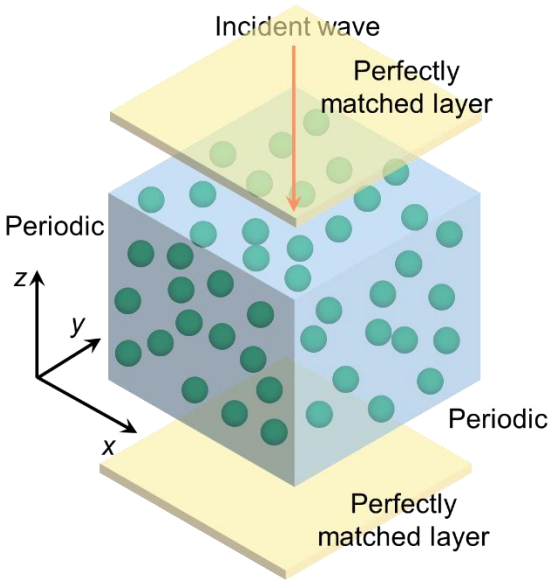

Figure S6. Schematic illustrating the domain and boundary conditions for the numerical simulation.

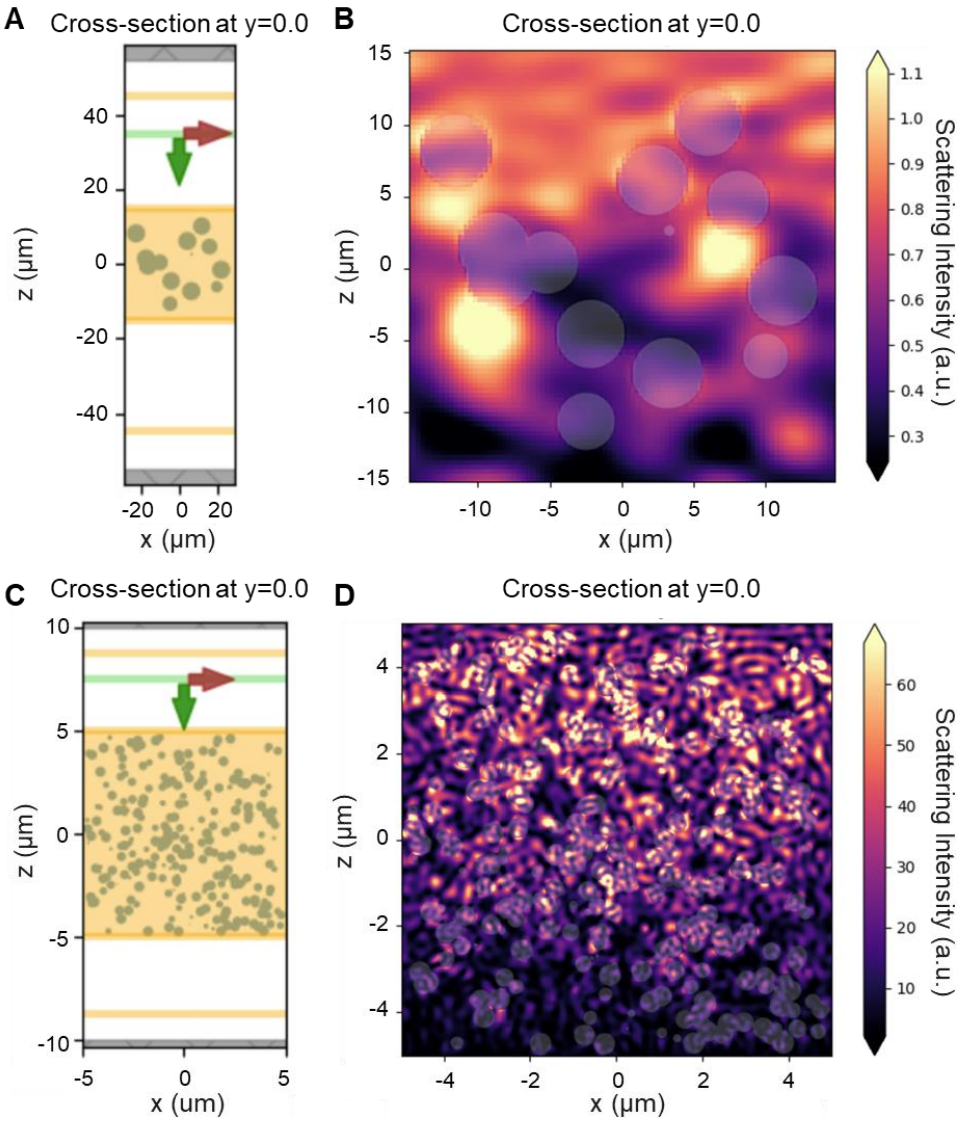

Figure S7. (**A**) Cross-sectional view of the simulation domain for SiO_2 particles, with a particle size of 5.0 μm and a volume fraction of 15%. (**B**) Distribution of the simulated electric field in the domain, depicted at the cross-section $y = 0.0$ for SiO_2 particles. (**C**) Cross-sectional view of the simulation domain for Al_2O_3 particles, with a particle size of 0.5 μm and a volume fraction of 30%. (**D**) Distribution of the simulated electric field in the domain, shown at the cross-section $y = 0.0$ for Al_2O_3 particles. For both SiO_2 and Al_2O_3 particles, our observations of the electromagnetic field distribution show that most particles primarily couple with themselves and the incident light, with minor particle-to-particle coupling.

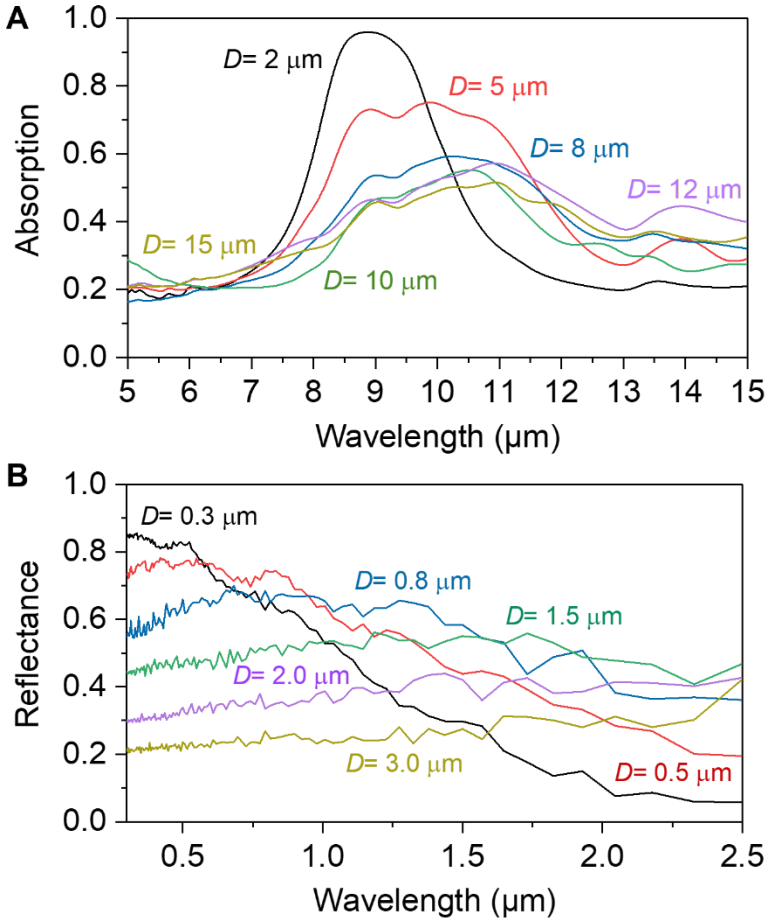

Figure S8. (**A**) Numerically simulated absorption for SiO_2 particles with varying sizes in the range of 5-15 μm. (**B**) Numerically simulated reflectance for Al_2O_3 particles with different sizes in the range of 0.3-2.5 μm. Comparative analysis between the spectra of randomly distributed particles and those of individual Al_2O_3 and SiO_2 particles (refer to Fig. S3A and Fig. S3D) reveals a consistent trend as particle diameters increase. This consistency validates the applicability of the Lorenz-Mie scattering theory for guiding the structural design of our radiative cooling glass coating.

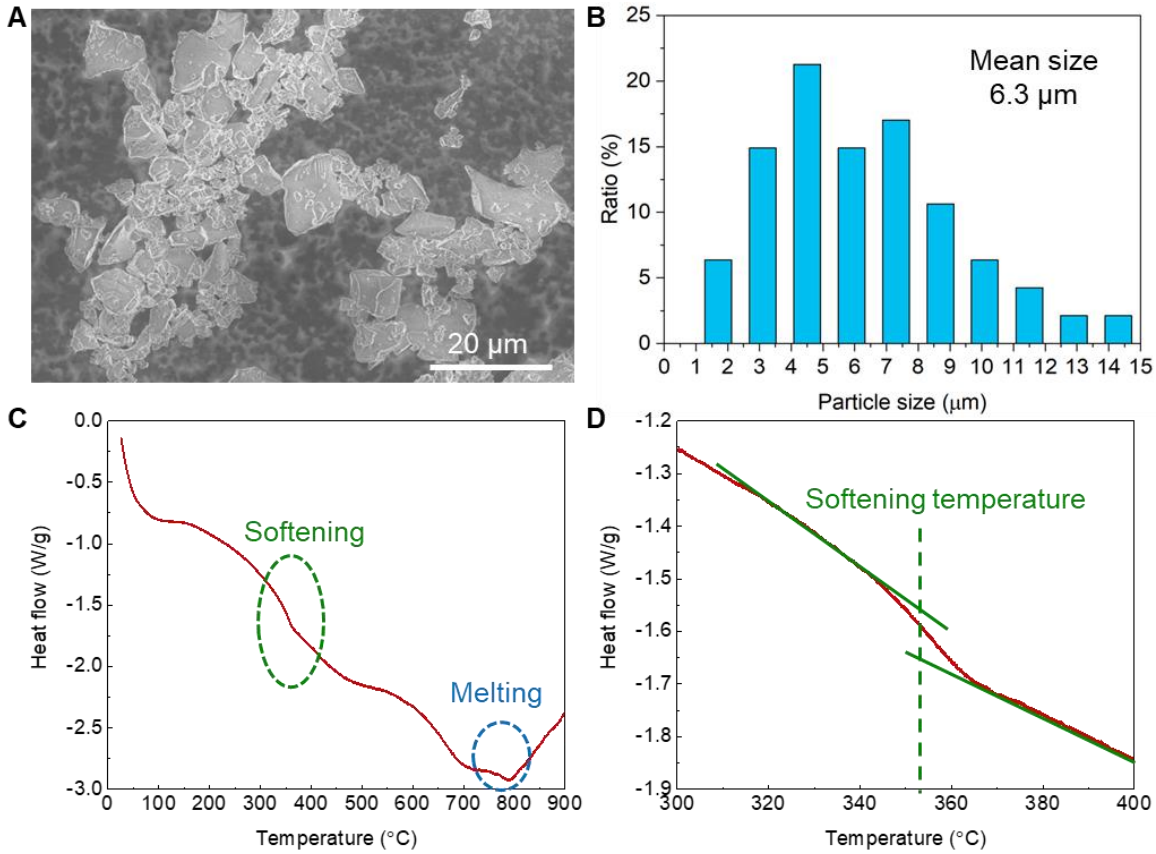

Figure S9. Characterization of the low-melting-point glass microparticles. (**A**) SEM image of the glass particles and (**B**) their corresponding diameter distribution. The size ranges from 2–15 μm with a mean particle size of 6.3 μm. (**C**) Differential scanning calorimetry (DSC) of the glass microparticles under air atmosphere. The heating rate was 10 °C/min. The softening process of glass occurs over a range of temperatures, specifically around 340-370°C. This is identified in DSC as a deviation in the heat flow profile, as opposed to a distinct peak that is characteristic of other transitions, such as melting. (**D**) Utilizing the half-height methodology, the change in heat flow observed around 352 °C is indicative of the softening temperature.

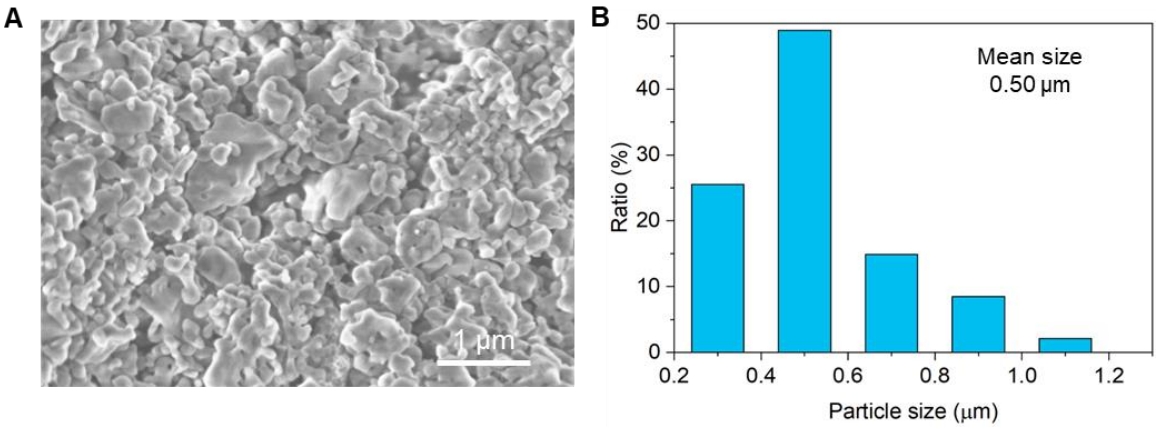

Figure S10. Characterization of the Al_2O_3 particles. (**A**) SEM image of the Al_2O_3 particles and (**B**) the corresponding diameter distribution.

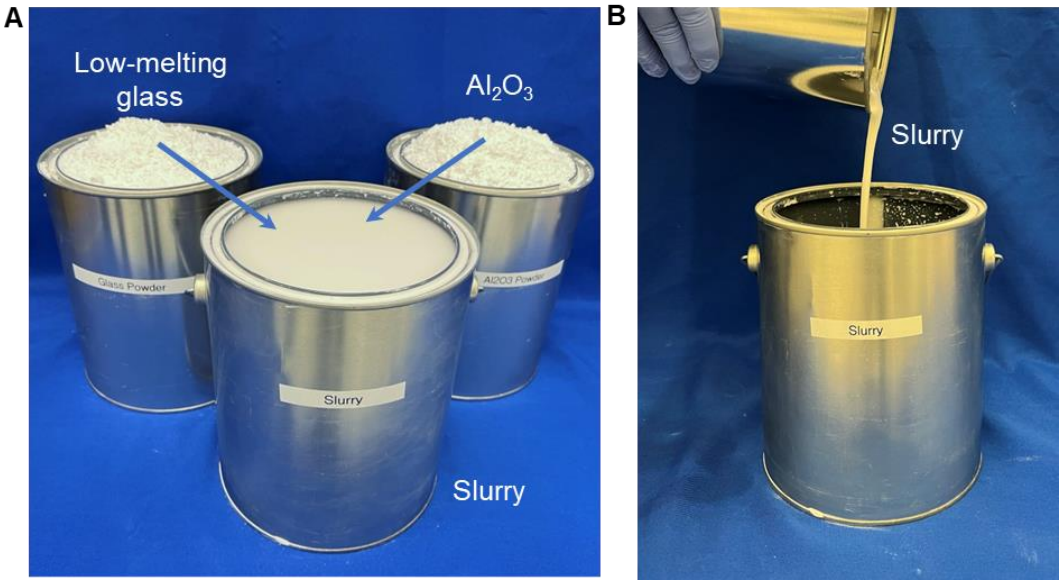

Figure S11. Raw materials used for preparing the radiative cooling glass coating. (**A**) The low-melting-point glass microparticles (2–15 μm) and Al_2O_3 nanoparticles (0.3–1.0 μm). (**B**) The slurry consists of a mixture of glass and Al_2O_3 particles suspended in ethanol, which demonstrates good fluidity.

Figure S12. Photograph showing that the glass/Al_2O_3 slurry can be brush-coated onto a ceramic tile.

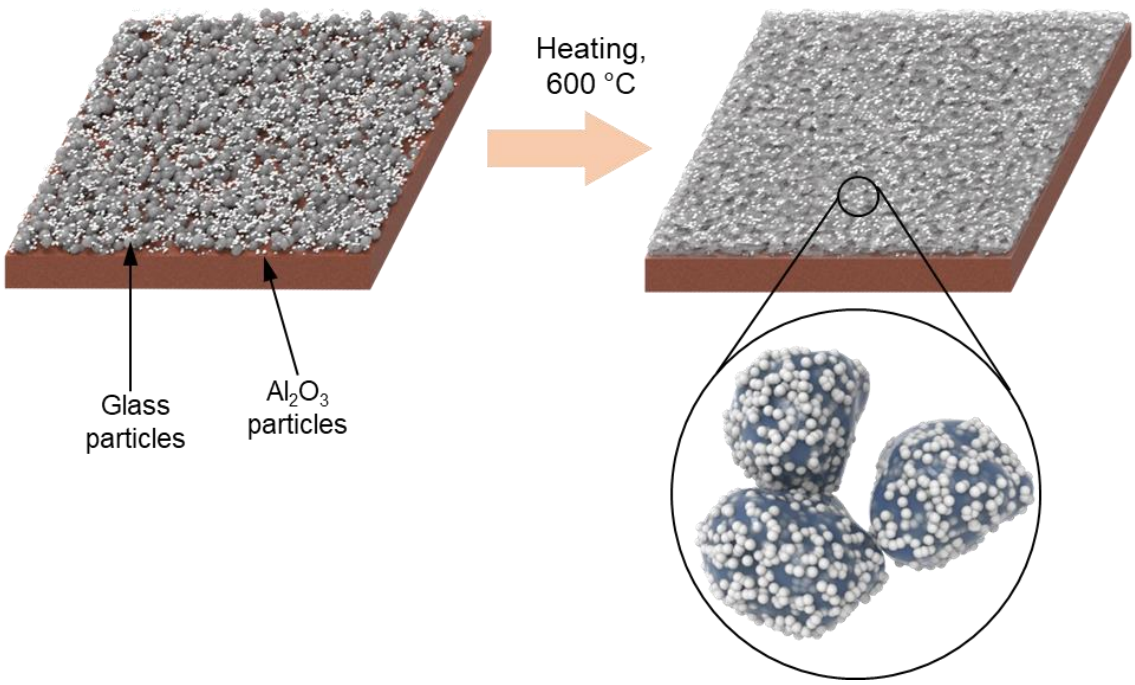

Figure S13. Schematic of the fabrication of the radiative cooling glass coating. By heating to ~600 °C, the low-melting-point glass microparticles in the mixture can be rapidly sintered to form an interconnected mesoporous structure.

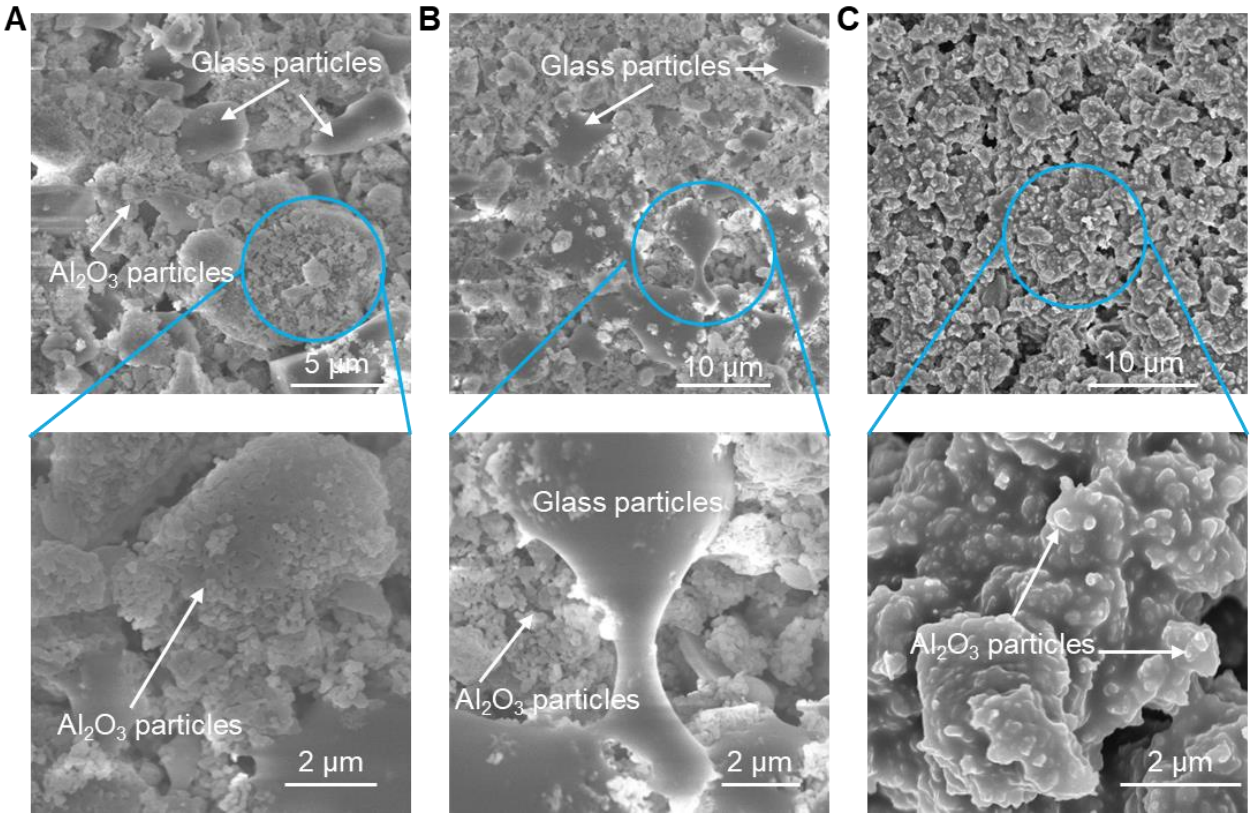

Figure S14. (**A**) SEM images of the glass and Al_2O_3 particles before sintering. (**B**) During sintering (600 °C, ~10 s), the high temperature causes the glass particles to soften and form necks. (**C**) After completing the sintering process, the glass particles bond together to form a porous network, with the Al_2O_3 particles wrapped by the glass.

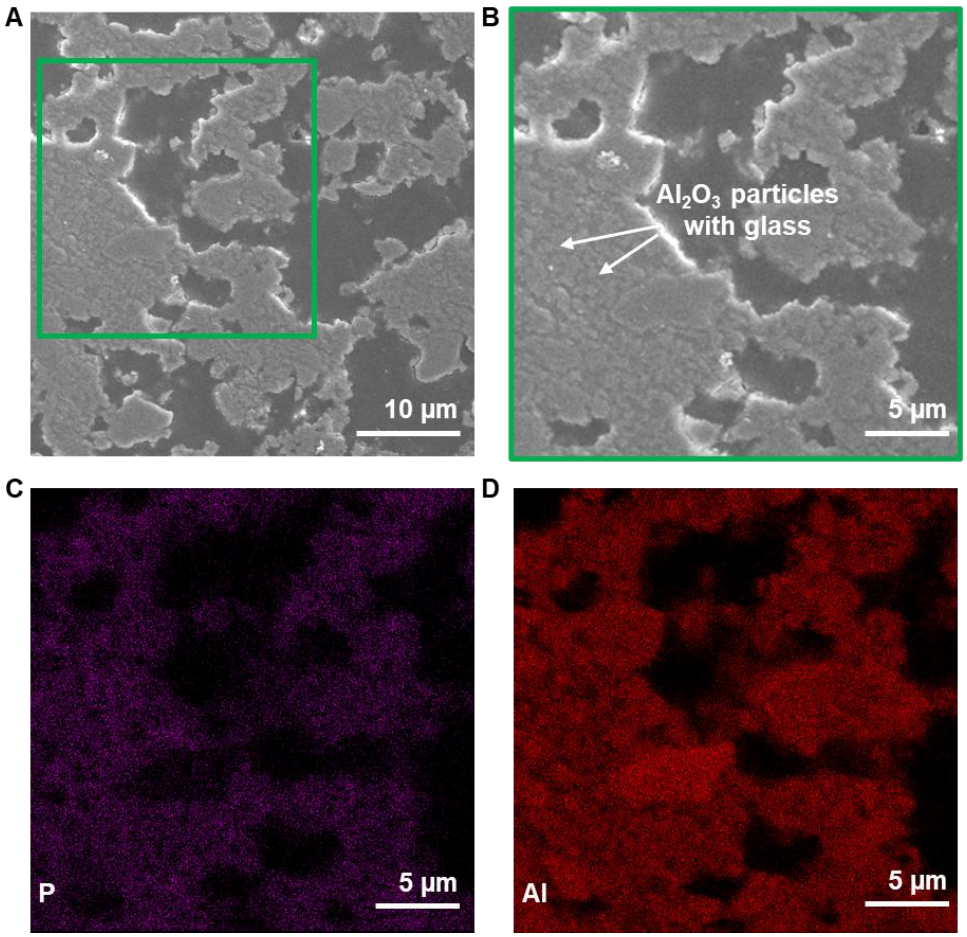

Figure S15. Characterization of the Al_2O_3 particle distribution in the sintered radiative cooling glass coatings. (**A**) SEM image illustrating the cross-sectional morphology of the microporous coating filled with polymeric resin (darker gray color). (**B**) The selected region for elemental mapping (EDS). The mapped distribution of (**C**) phosphorus, serving as an indicator for glass particles, and (**D**) aluminum elements, serving as an indicator for Al_2O_3 particles, in the radiative cooling glass coatings.

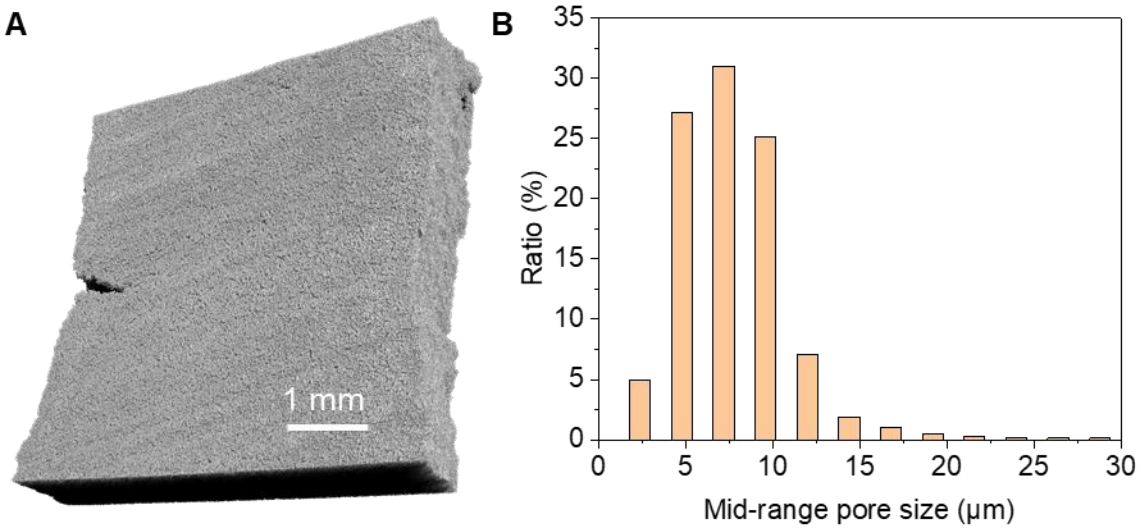

Figure S16. Microstructural visualization and pore size distribution of the radiative cooling glass coating, as determined by Micro-CT. The pore size distribution gauged by Micro-CT aligns closely with our SEM observations. Micro-CT results highlight a porosity of 49.5% and an average pore size of 7.94 ± 4.91 μm. These findings are consistent with our SEM observations, which reported a porosity of approximately 50% and an average pore size of 6.7 μm (Fig. 2H).

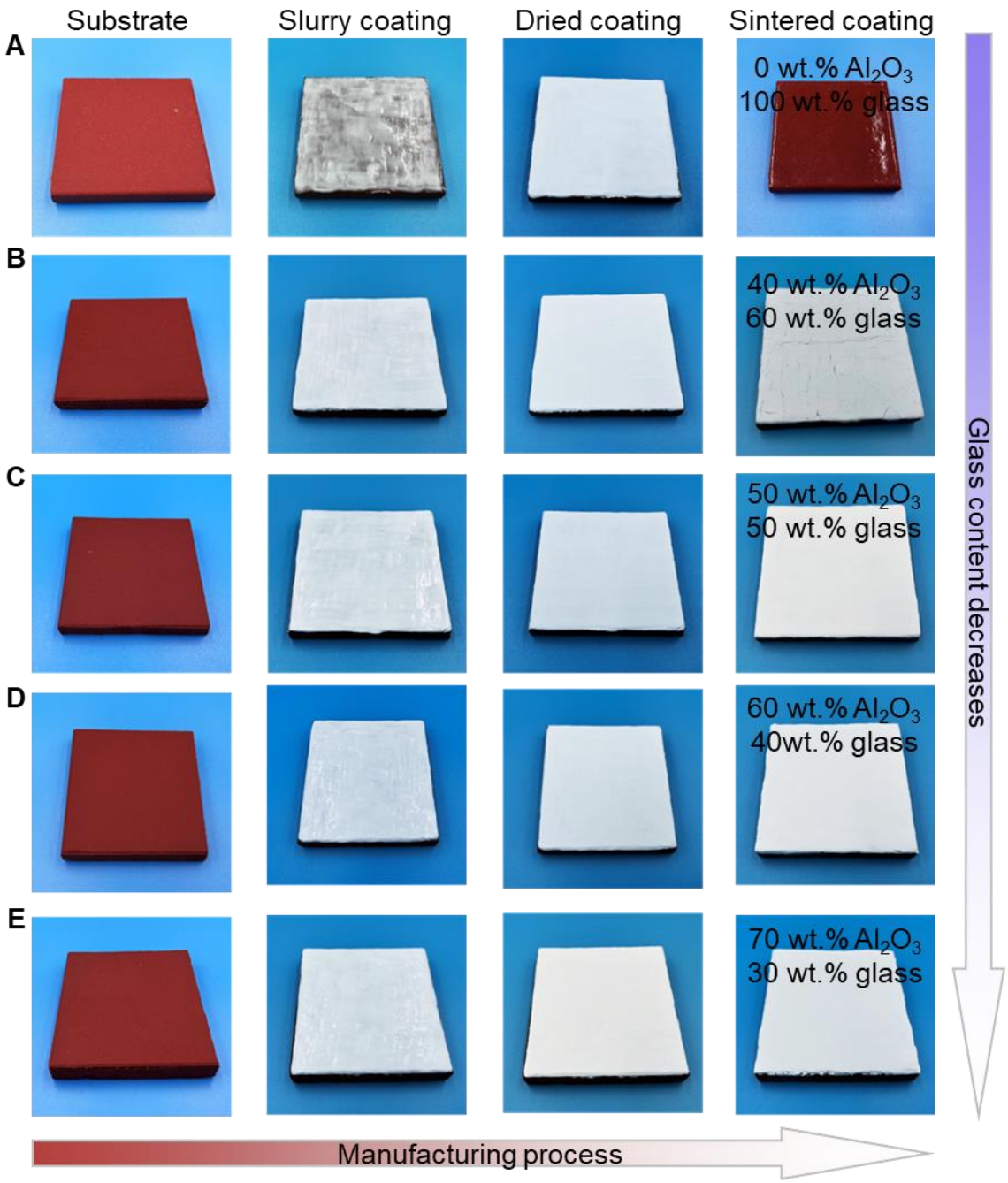

Figure S17. Photographs of radiative cooling glass coatings fabricated using different Al_2O_3 contents, including: (**A**) 0 wt.% Al_2O_3 and 100 wt.% glass, (**B**) 40 wt.% Al_2O_3, and 60 wt.% glass, (**C**) 50 wt.% Al_2O_3 and 50 wt.% glass, (**D**) 60 wt.% Al_2O_3 and 40 wt.% glass, and (**E**) 70 wt.% Al_2O_3 and 30 wt.% glass. Without Al_2O_3 particles, the glass microparticles aggregate and form a transparent structure. When the mass fraction of the Al_2O_3 particles increases to 40 wt.%, the radiative cooling glass turns more opaque white, indicating a relatively high solar reflectance. However, the sintered structure is fragile and easily breaks during the cooling process. As the mass fraction of the Al_2O_3 particles increases to 50 wt.%, the radiative cooling glass structure appears very white, indicating a high solar reflectance. Meanwhile, the structure is uniform and free of

cracks. When we increased the mass fraction of Al_2O_3 particles to 60 wt.% and 70 wt.%, the radiative cooling glass coatings appear white and show high solar reflectance. However, when the mass fraction of Al_2O_3 is larger than 60 wt.%, the coatings begin to easily erode off the substrate, indicating a lower adhesion strength. These results suggest that the optimal mass fraction of Al_2O_3 particles is in the range of 40–60 wt.%.

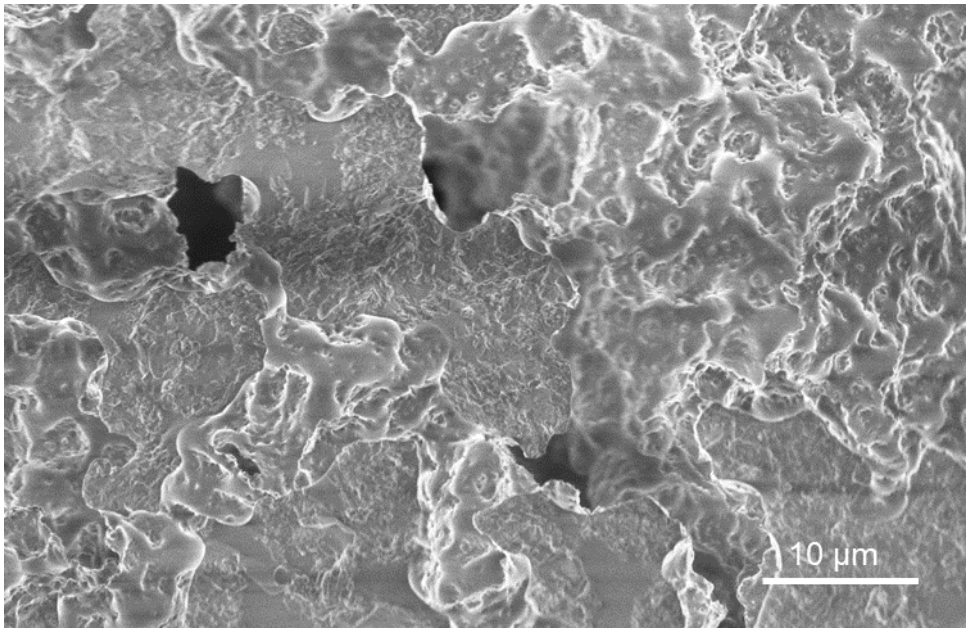

Figure S18. SEM image of the cross-sectional morphology of the coating with a glass content of 40 wt.%, showing a much lower porosity compared with the coating with a glass content of 50 wt.% (Figs. 2F, 2G).

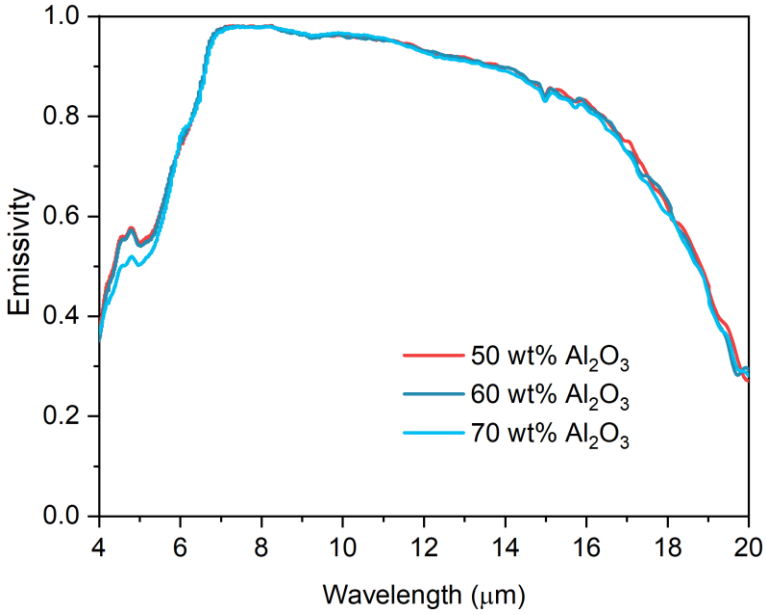

Figure S19. Effect of the mass fraction of Al_2O_3 particles on the infrared emissivity of the radiative cooling glass coating with a thickness of ~550 μm.

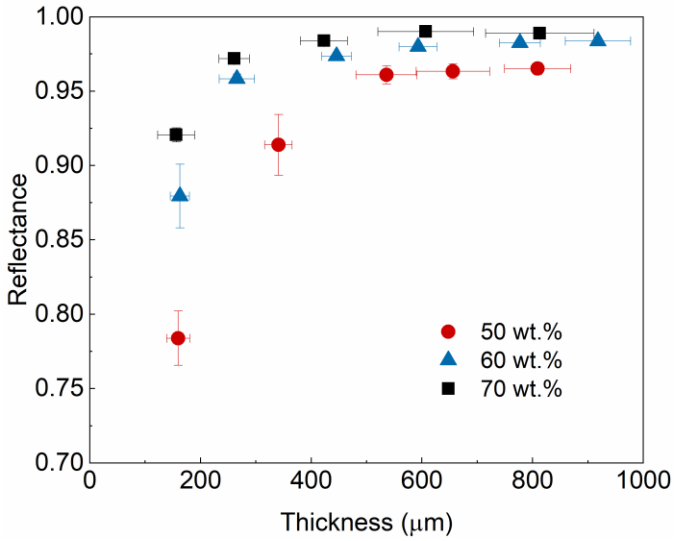

Figure S20. Solar reflectance of brush-coated radiative glass coatings with Al_2O_3 mass fractions of 50 wt.%, 60 wt.%, and 70 wt.%, as a function of coating thickness.

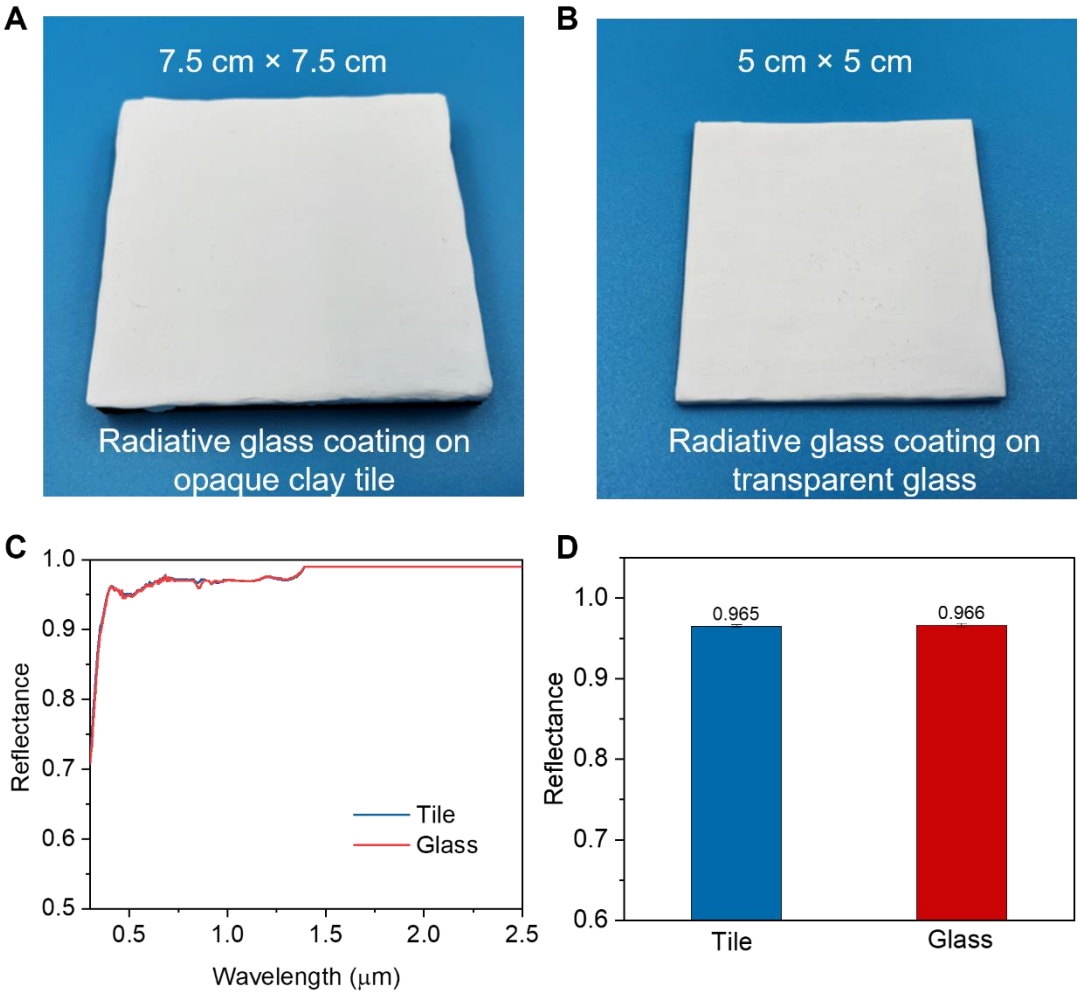

Figure S21. Comparison of the solar reflectance of the cooling glass coating (thickness of ~550 μm) on opaque clay tile and transparent glass substrates. Photographs of the radiative cooling glass coating on an (**A**) opaque ceramic tile and (**B**) transparent glass substrate. (**C**) Comparison of the spectral solar reflectance of the cooling glass coatings on the ceramic tile and glass. (**D**) Comparison of the average solar reflectance of the radiative cooling glass coatings on the ceramic tile and glass. The results show that the solar reflectance of the cooling glass coating is independent of the substrate.

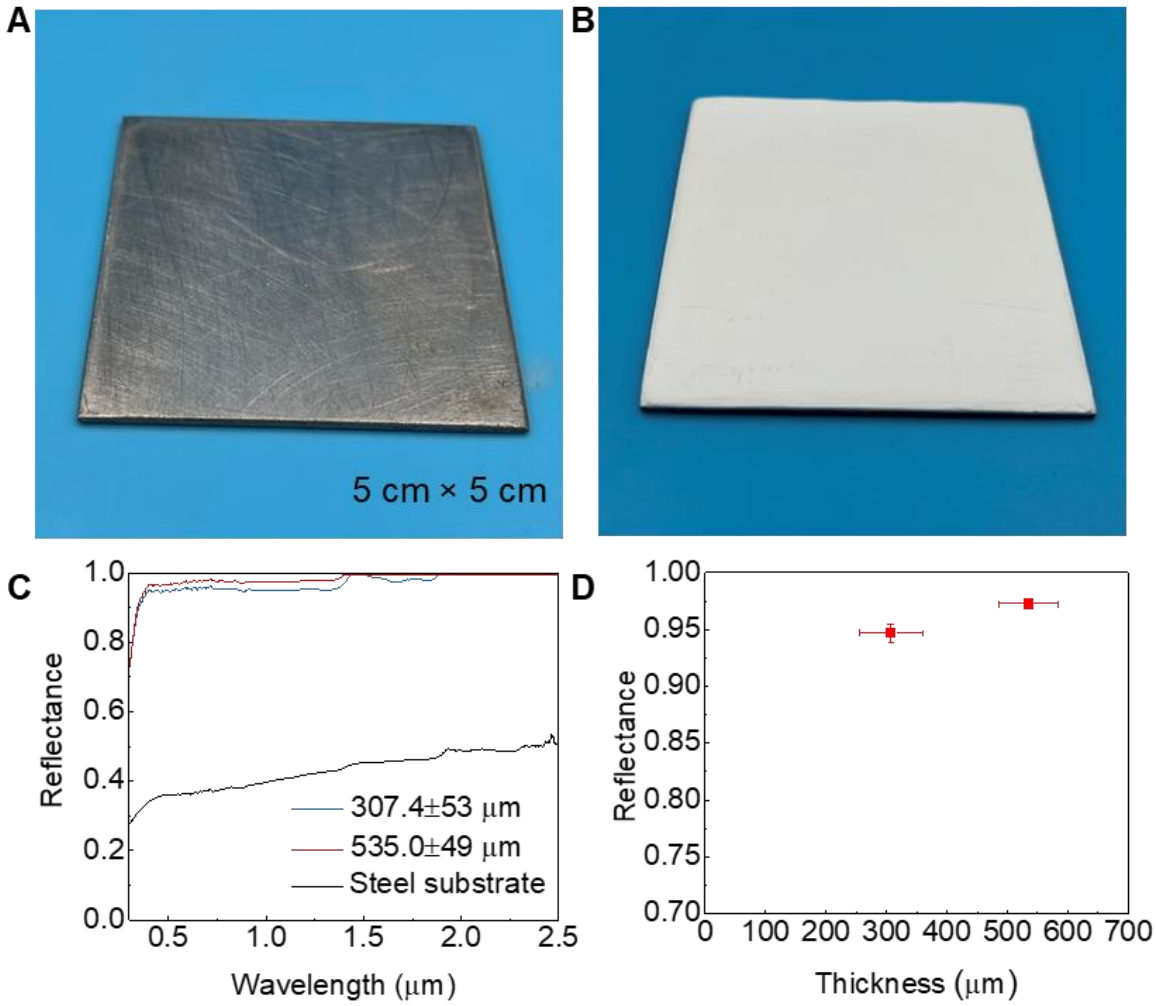

Figure S22. Illustration of the radiative cooling glass on a steel substrate. (**A**) Photograph of the bare steel substrate and (**B**) the same substrate coated with radiative cooling glass. (**C**) Spectral reflectance of the steel substrate when coated with radiative cooling glass coatings of different thicknesses across the solar range (0.3-2.5 μm). (**D**) Averaged solar reflectance of the steel substrate coated with radiative cooling glass, showcasing variations in thickness.

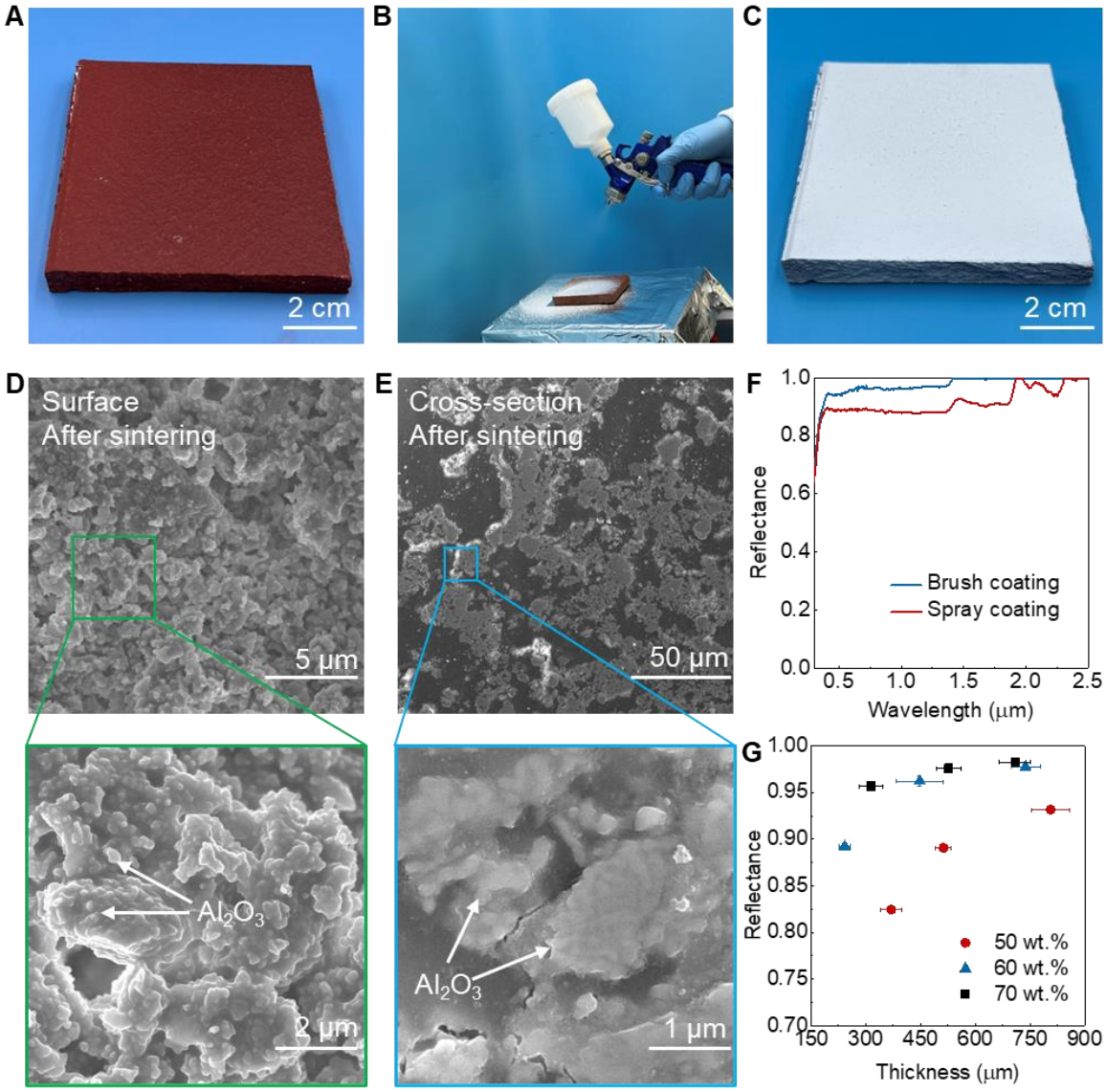

Figure S23. Demonstration of the application of radiative cooling glass coatings on ceramic tiles using a spray coating method. Photographs of (**A**) the ceramic tile before application, (**B**) the spray coating process, and (**C**) the ceramic tile after being coated with the radiative cooling glass coating. SEM images of the (**D**) surface and (**E**) cross-sectional morphology of the sintered radiative cooling glass coating applied through the spray coating process. (**F**) Comparison of the reflectance between the radiative cooling glass coatings fabricated through brush coating (505 ± 55 μm, 0.951 ± 0.006) and spray coating (513 ± 21 μm, 0.891 ± 0.003). The mass fraction of Al_2O_3 in these comparisons is 50 wt.%. (**G**) The solar reflectance of spray-coated radiative glass coatings with Al_2O_3 mass fractions of 50 wt.%, 60 wt.%, and 70 wt.%, plotted as a function of coating thickness.

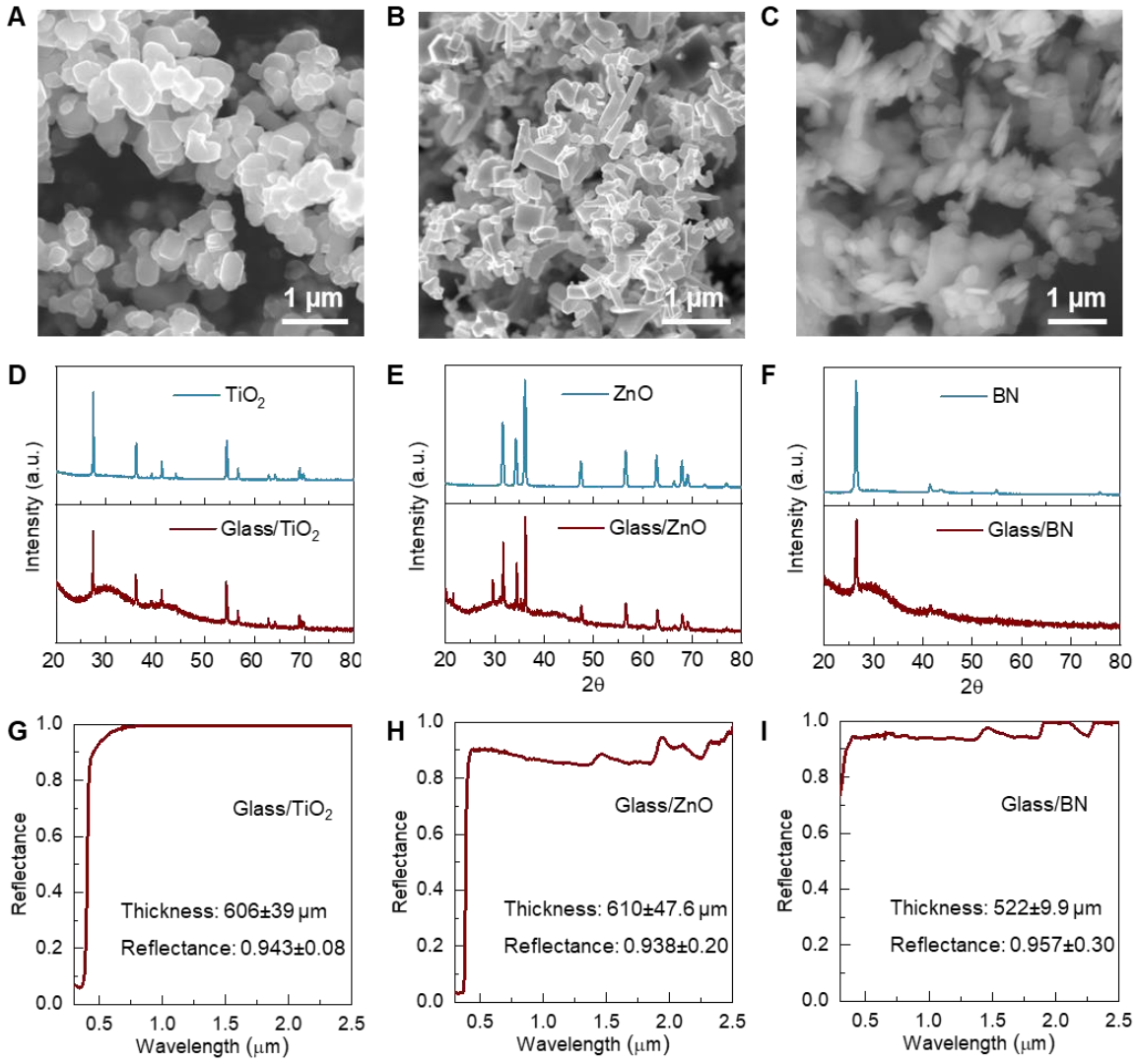

Figure S24. SEM image of the (**A**) TiO_2 particles, (**B**) ZnO particles, and (**C**) BN disks, with a mean diameter of ~0.5 μm. XRD patterns of the glass coatings sintered using (**D**) TiO_2, (**E**) ZnO, and (**F**) BN particles as sunlight scatterers. Solar reflectance of the glass coating employing (**G**) TiO_2, (**H**) ZnO, and (**I**) BN particles as sunlight scatterers.

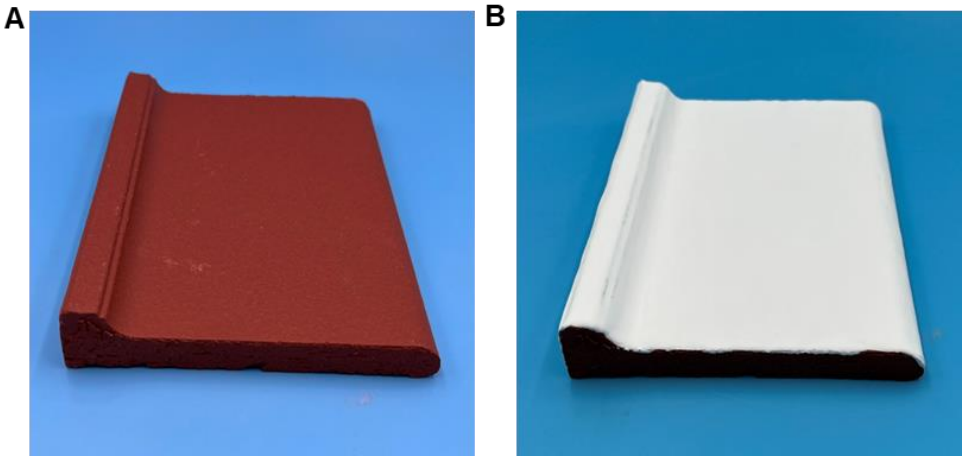

Figure S25. Photographs of (**A**) a curved tile, subsequently applied with (**B**) radiative cooling glass.

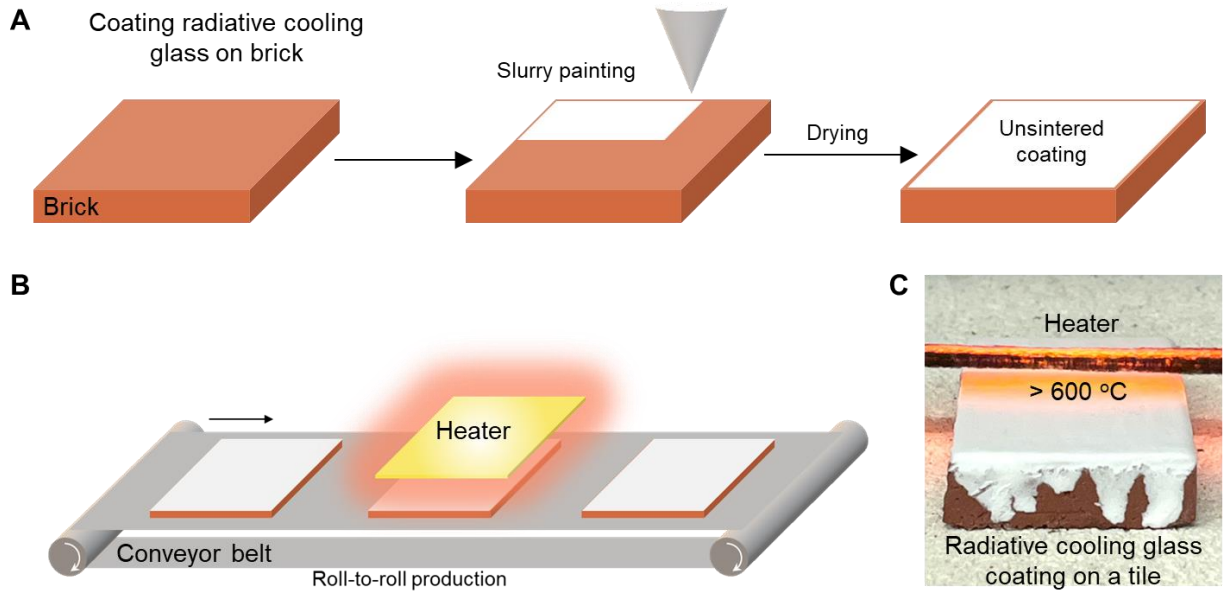

Figure S26. Large-scale production of radiative cooling glass coating on ceramic tiles via a roll-to-roll process. (**A**) Illustration of slurry painting on a ceramic tile. (**B**) Roll-to-roll production of the radiative cooling glass coating on a substrate. The radiative cooling glass-coated tiles move through the heating zone. The heating temperature and duration can be controlled by adjusting the heating power and roller speed, respectively. (**C**) A demonstration of the heating process to fabricate the radiative glass coating via a high-temperature heater. The dried powders on the ceramic tile are rapidly heated to ~600 °C or higher to be sintered into the radiative cooling glass coating.

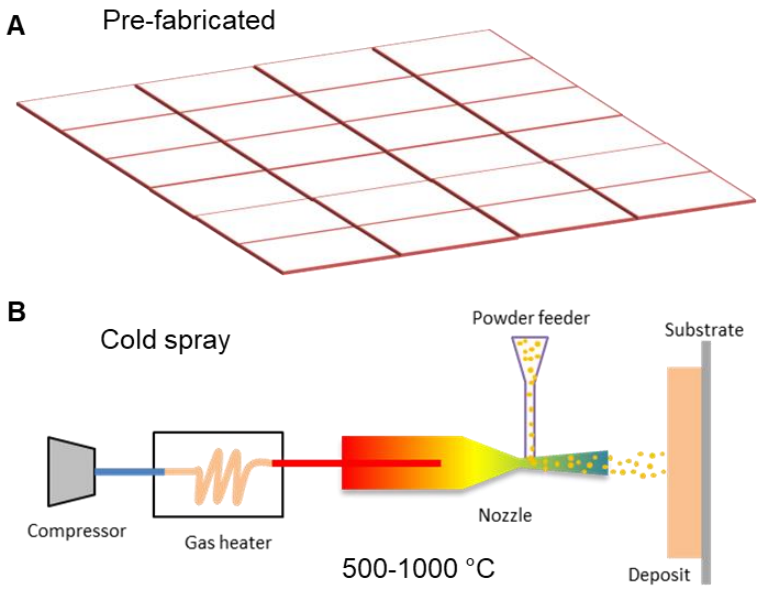

Figure S27. Illustration of potential large-scale applications. (**A**) Diagram illustrating the glass coating pre-applied to a substrate, suitable for large-scale implementation. (**B**) Conceptual outline of the on-site coating process utilizing cold spray technology. (*70*).

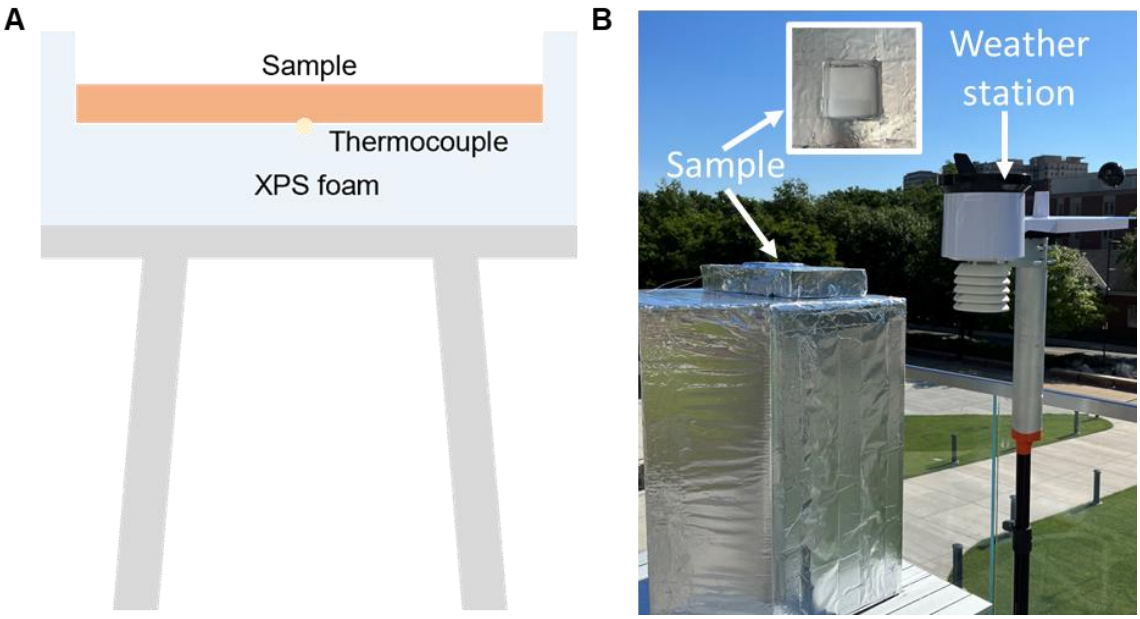

Figure S28 (**A**) Schematic of the setup for the real-time measurement of the sub-ambient cooling performance. T-type thermal couples with an accuracy of ± 0.5 °C were placed beneath the sample coated with the radiative cooling glass for temperature measurement. To minimize parasitic heat loss from the system to the surroundings, the samples were surrounded by thermally insulating extruded polystyrene foam (i.e., XPS). (**B**) Photograph of the setup for the real-time measurement of the sub-ambient cooling performance. The inset image displays a top-down view of the setup. To reduce the effect of solar heating on the measurements, the XPS insulation materials were covered with aluminum foil. The setup was raised ~1.5 m to avoid heat transfer from the roof.

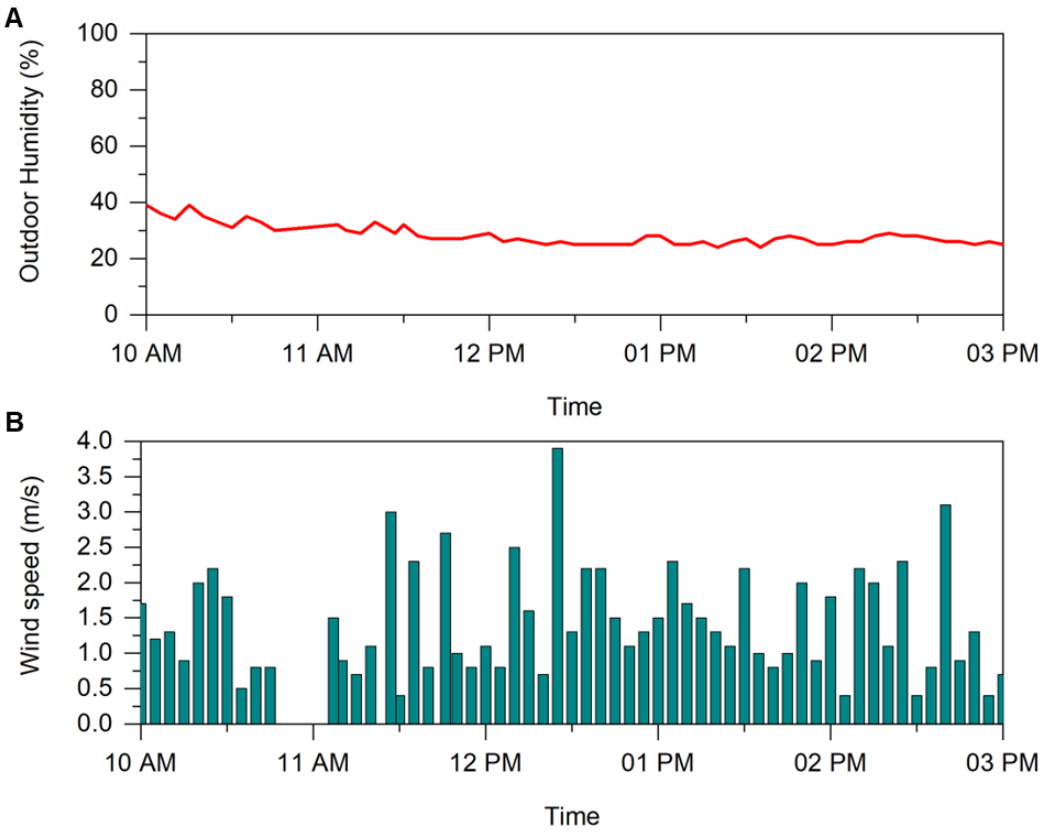

Figure S29. Outdoor (**A**) humidity and (**B**) wind speed during the daytime measurement.

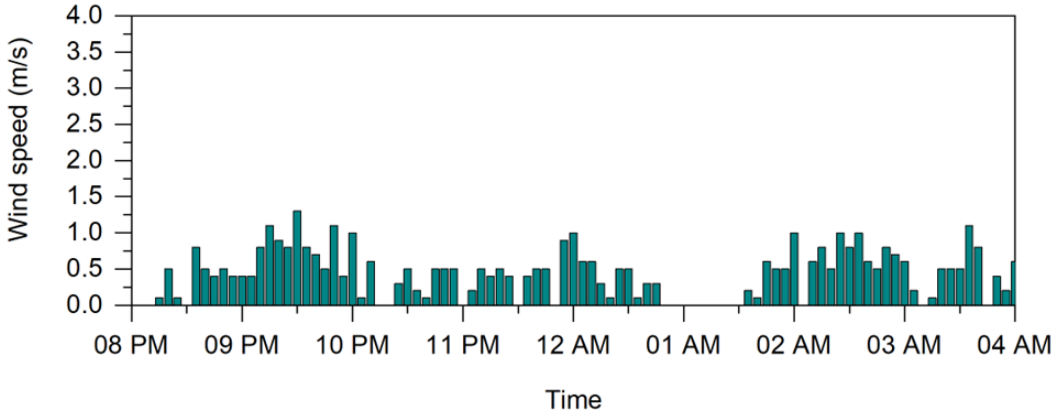

Figure S30. The wind speed during the nighttime measurement.

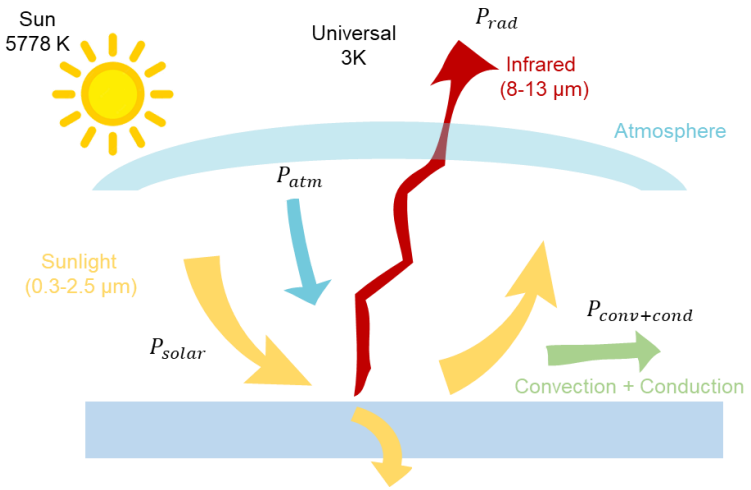

Figure S31. Schematic illustration of the energy balance for a panel exposed to a clear sky during daytime. The net energy absorbed by the panel is influenced by multiple factors, including the incident solar irradiance, ambient temperature, wind speed, and the panel's solar reflectance.

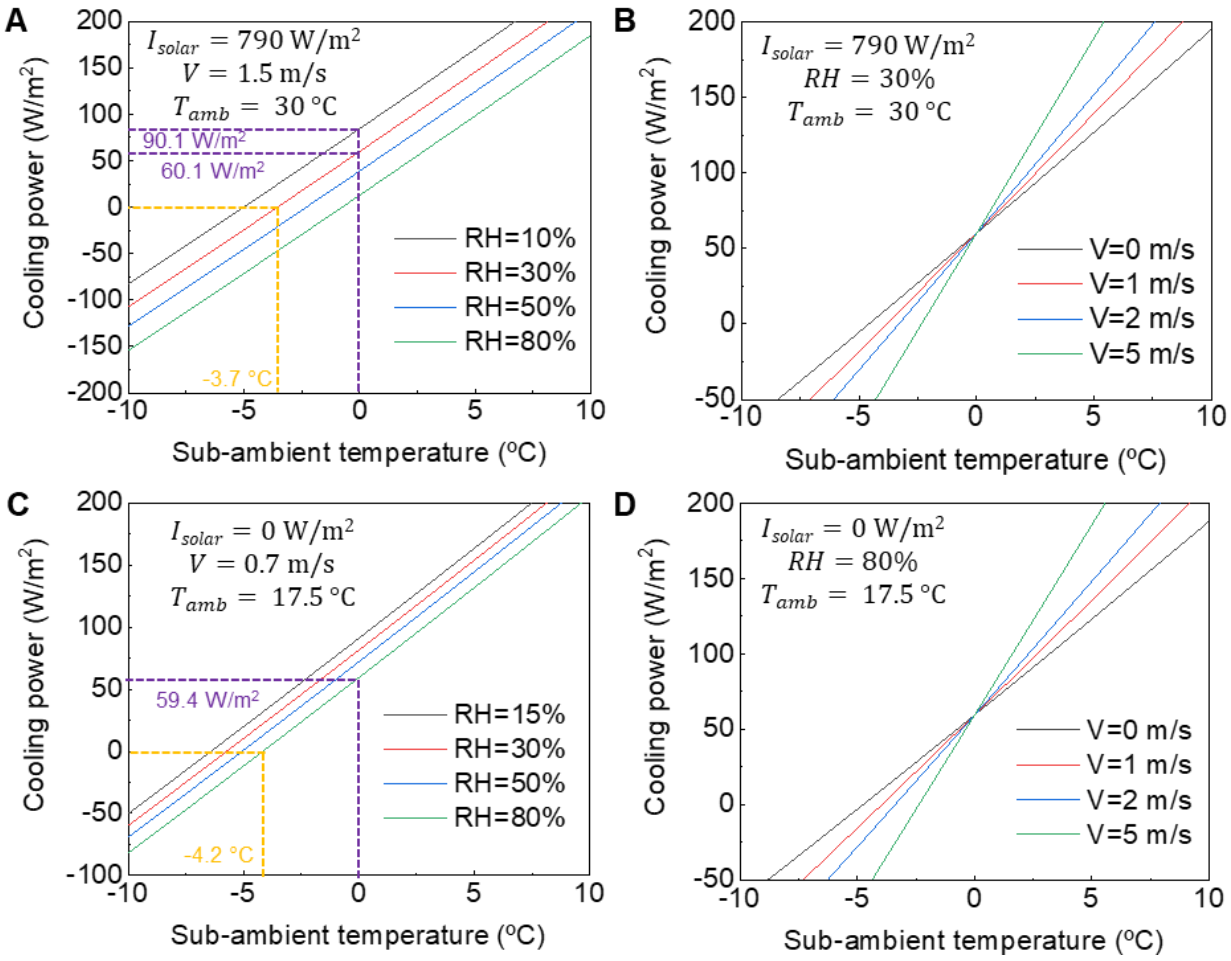

Figure S32. Analysis of the net cooling power ($P_{net}(T)$) and sub-ambient temperature ($T - T_{amb}$) for the glass coating under diverse conditions. (**A-B**) The cooling power relative to the cooler's sub-ambient temperature at noontime, accounting for the impact of (**A**) humidity and (**B**) wind speed. Here, the ambient temperature is set at 30 °C with a solar irradiance of 790 W/m^2. (**C-D**) The cooling power in relation to the cooler's sub-ambient temperature during nighttime, with an ambient temperature of 30 °C and solar irradiance of 0 W/m^2, accounting for the impact of (**C**) humidity and (**D**) wind speed. During both noontime and nighttime scenarios, our model's predictions of approximately 3.7 °C and 4.2 °C temperature drop closely align with our empirical observations of 3.5 °C and 4 °C, respectively. The projected cooling power during both daytime and nighttime is ~60 W/m^2.

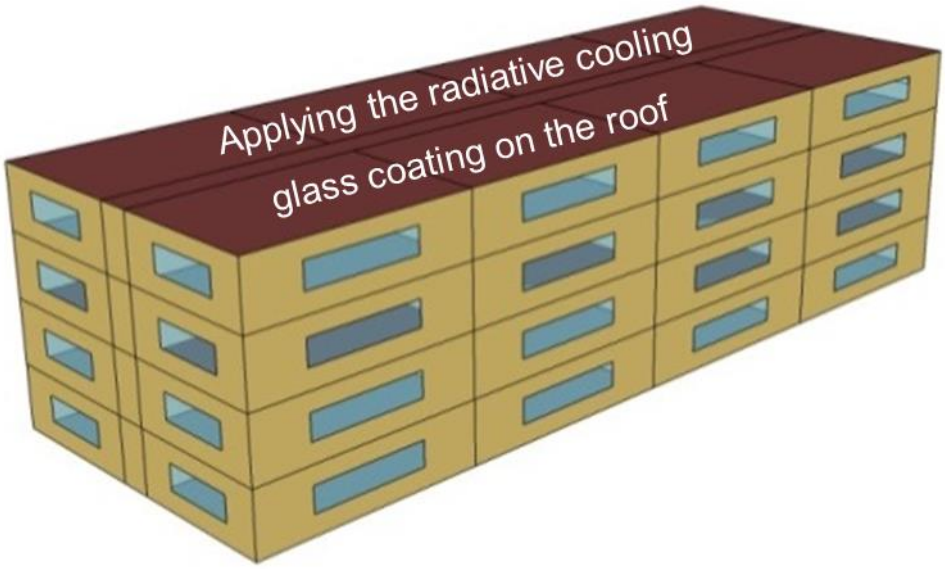

Figure S33. Geometric structure of the simulated midrise apartment building, which has a floor area of 3135 m^2 (4 floors), roof area of 783 m^2, external wall surface of 1542 m^2, and window-to-wall ratio of 20%.

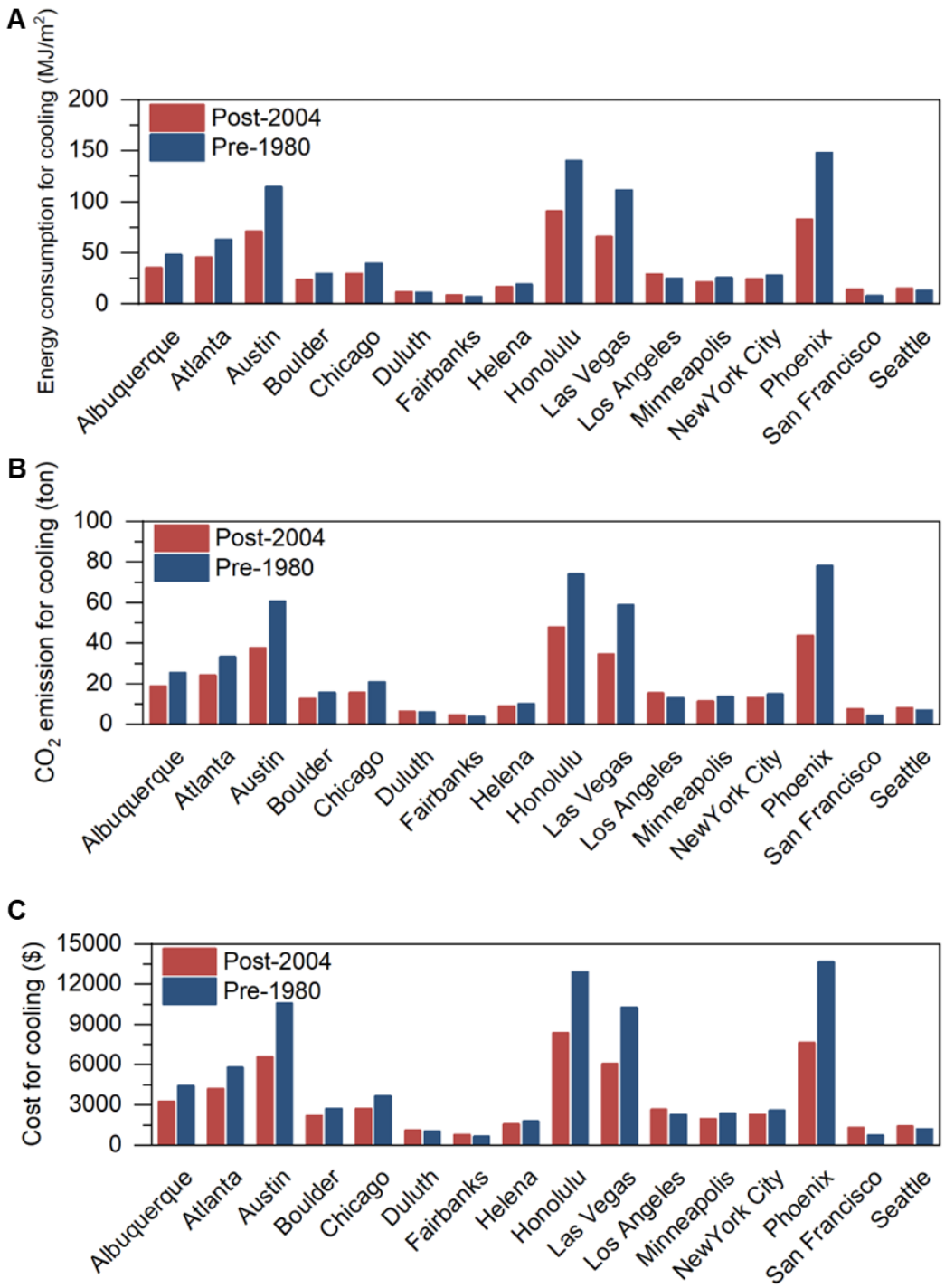

Figure S34. Annual (**A**) energy consumption, (**B**) CO_2 emission, and (**C**) cost for cooling the DOE Pre-1980 and Post-2004 reference midrise apartment buildings in 16 representative cities in the United States, serving as a baseline for comparison.

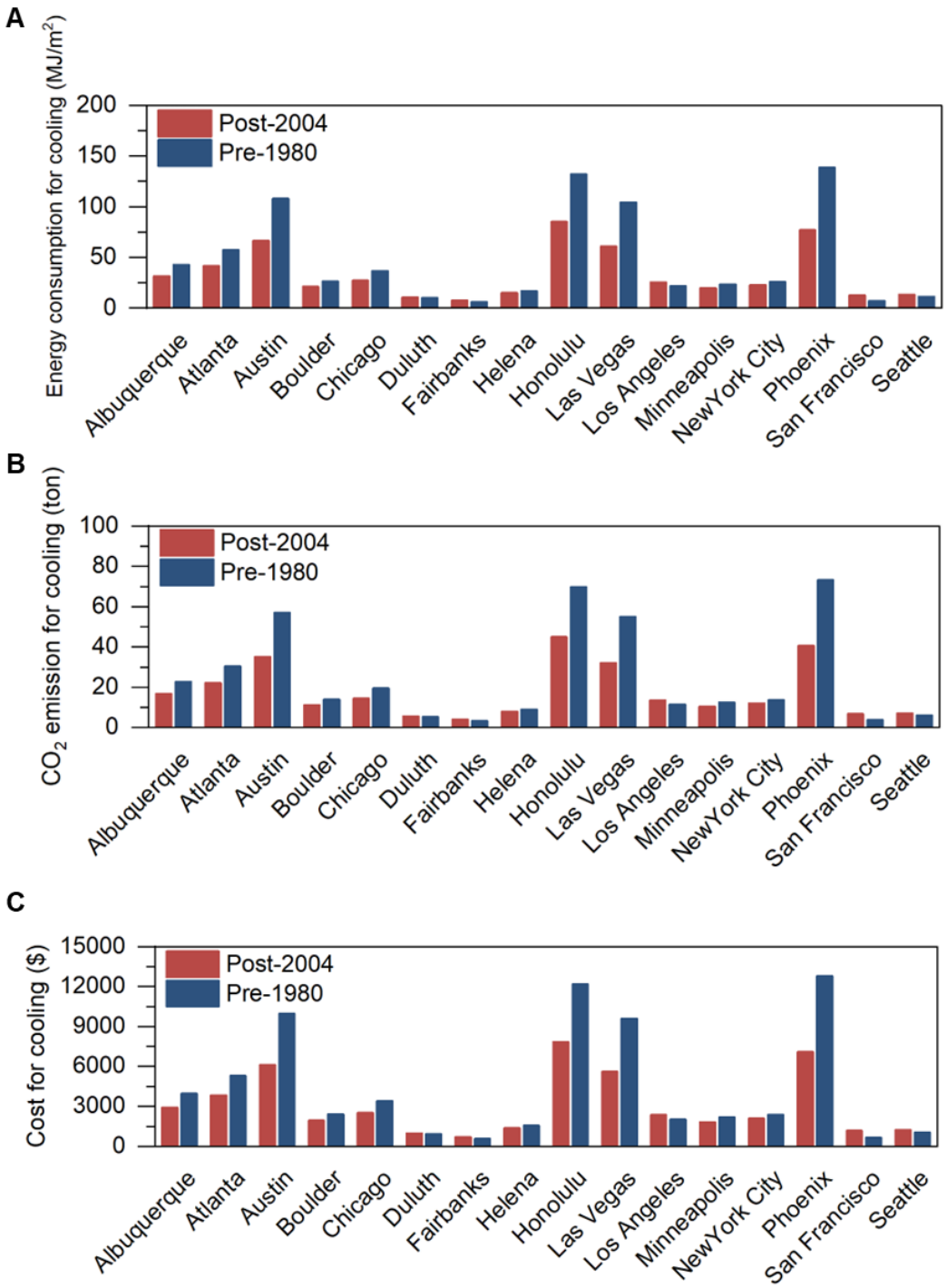

Figure S35. Annual (**A**) energy consumption, (**B**) CO_2 emission, and (**C**) cost for cooling the Pre-1980 and Post-2004 reference midrise apartment buildings when the cooling glass coating is applied to the roof.

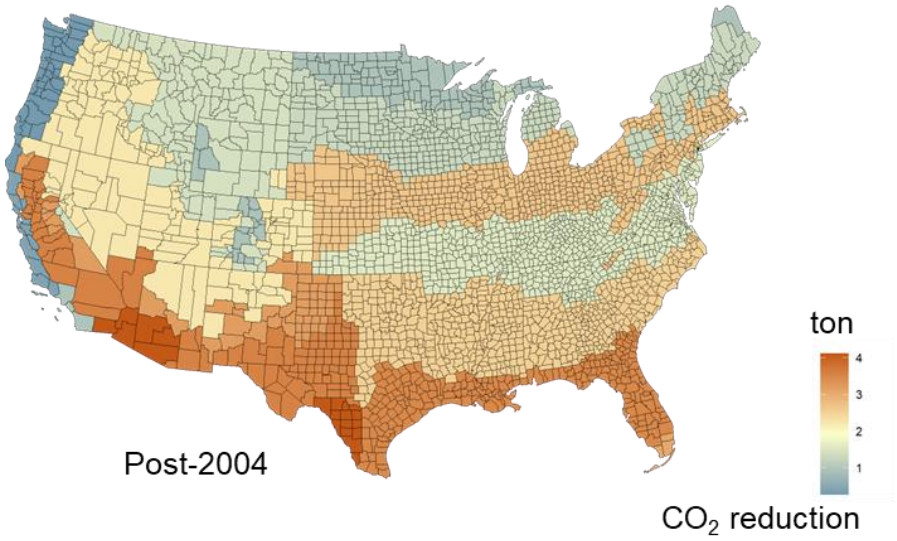

Figure S36. Annual CO_2 reduction for cooling Post-2004 midrise apartment buildings in U.S. cities with the cooling glass coating applied to the roof.

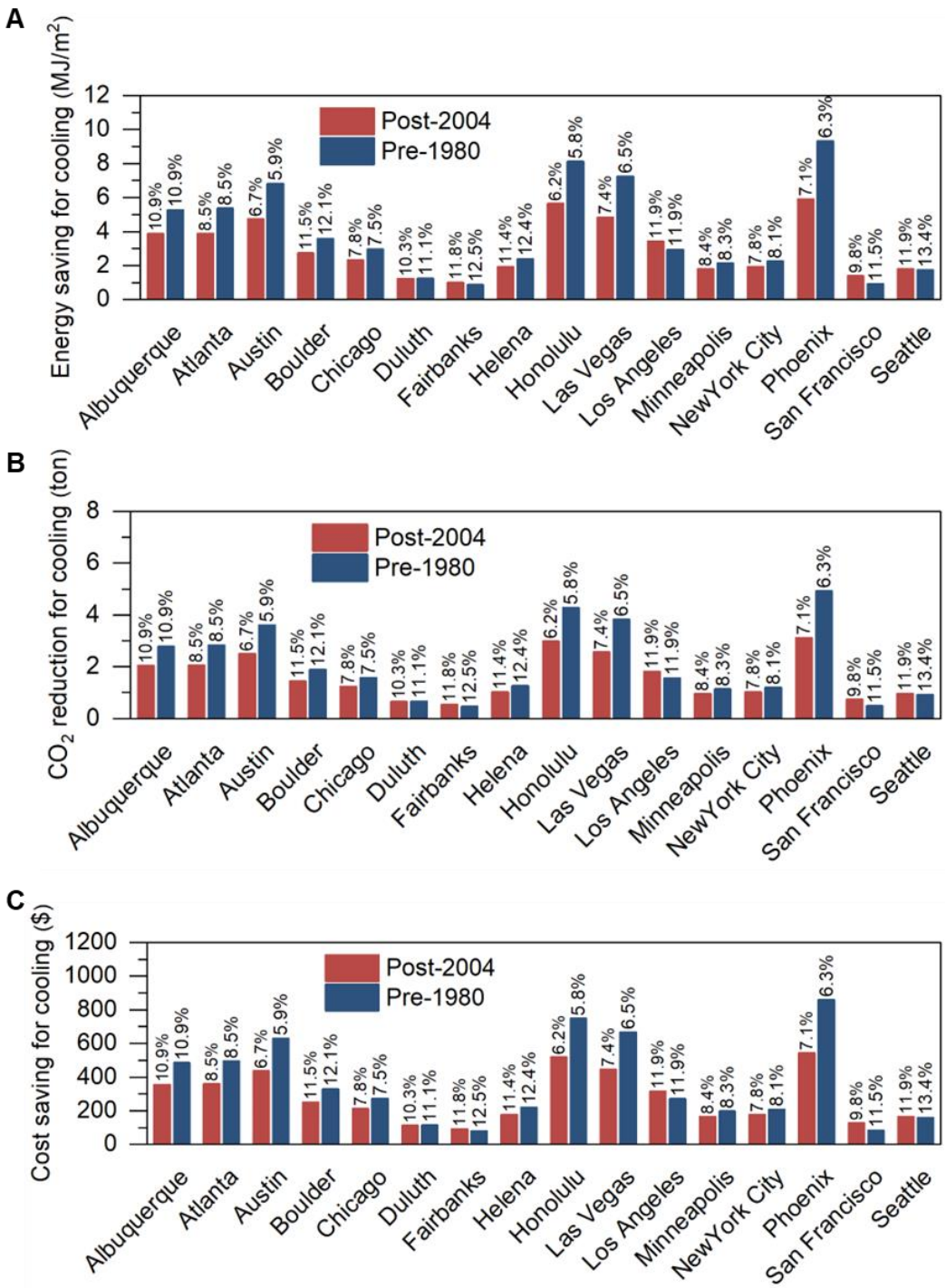

Figure S37. Annual (**A**) energy savings, (**B**) CO_2 emission reductions, and (**C**) cost savings for cooling the Pre-1980 and Post-2004 reference midrise apartment buildings when the radiative cooling glass coating is applied on the roof.

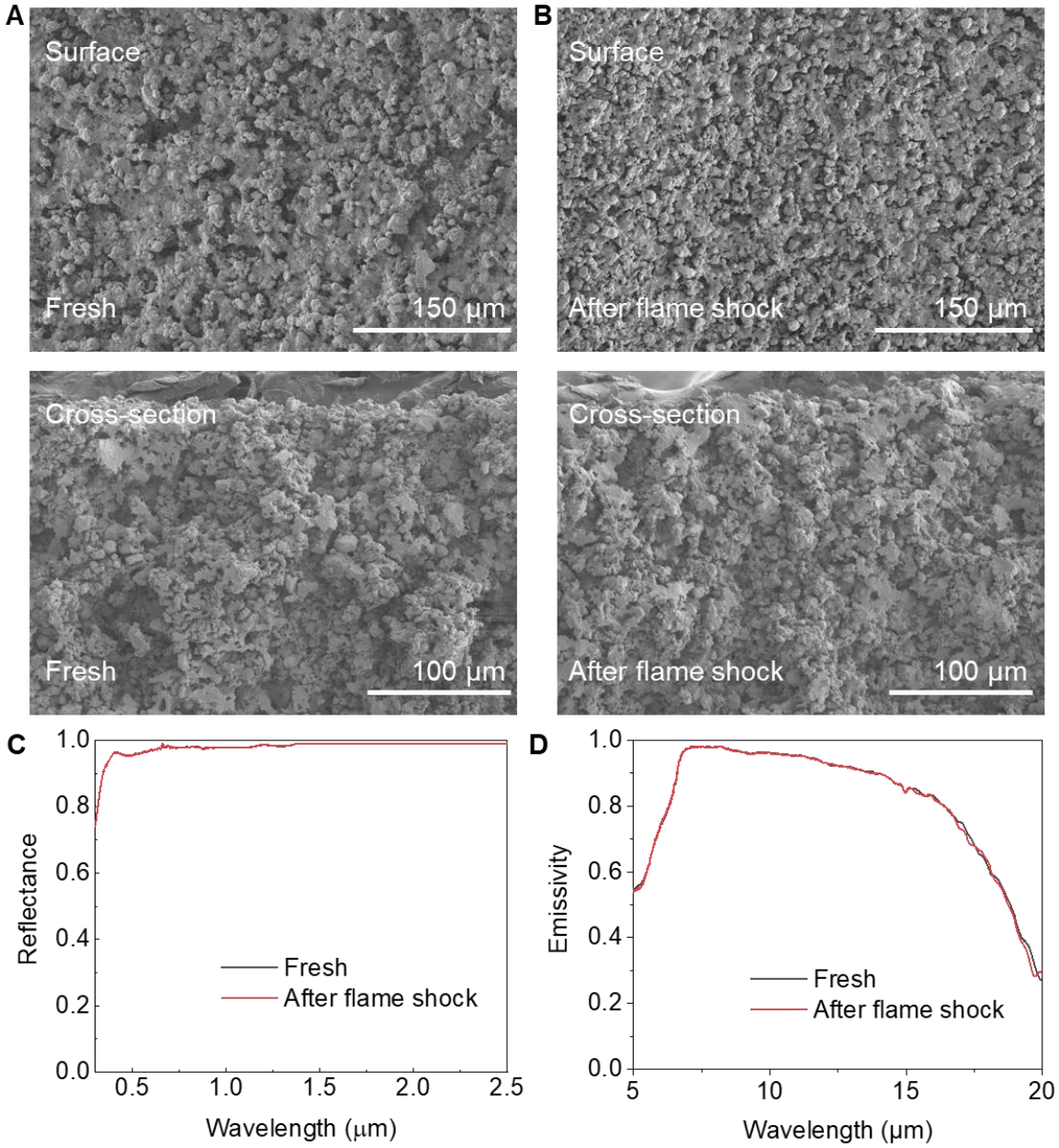

Figure S38. Comparison of the microstructures and optical performance of the radiative cooling glass coating before and after high-temperature flame shock (up to 1000°C, 10s). (**A**) SEM image showing the surface and cross-sectional micro-morphology of the fresh radiative cooling glass coating. (**B**) SEM image of the surface and cross-sectional micro-morphology of the radiative cooling glass coating after thermal shock. (**C**) Comparison of the spectral reflectance in the solar region (0.3-2.5 μm) for the fresh and post-flame shock radiative glass coatings. (**D**) Comparison of the infrared emissivity (5-20 μm) for the fresh and post-flame shock radiative glass coatings.

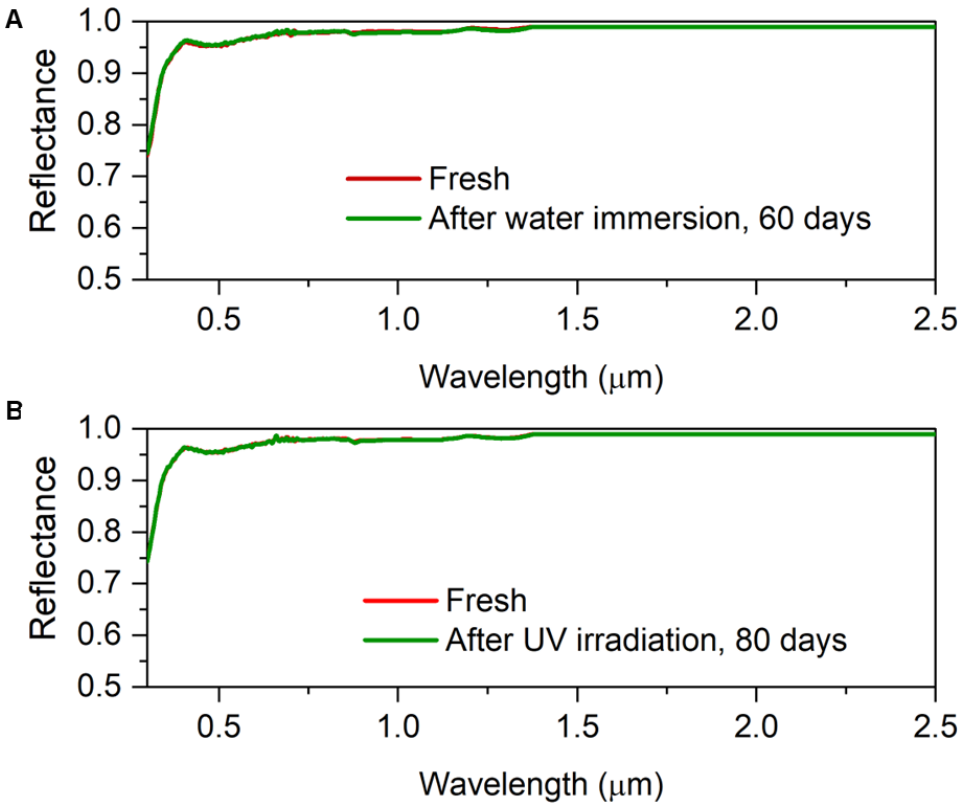

Figure S39. Comparison of the solar reflectance of the radiative cooling glass coatings after (**A**) immersion in water for 60 days, and (**B**) UV irradiation for 80 days. No obvious changes in the solar reflectance were observed.

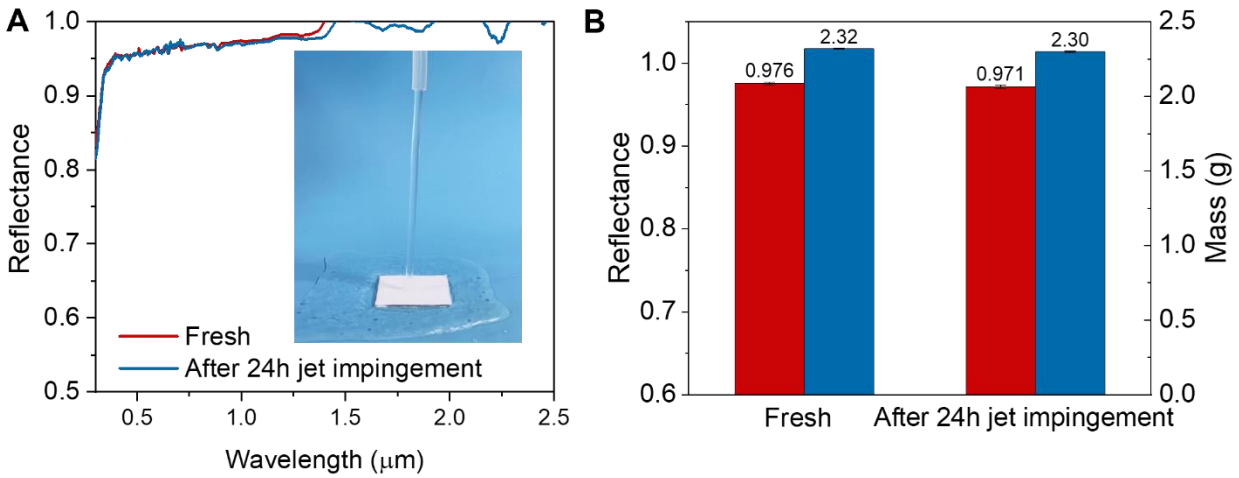

Figure S40. Comparison between the (**A**) solar reflectance and (**B**) mass of the fresh sample after 24 hours of jet impingement. The impingement force was estimated to be ~ 4 N, which is much higher than the impacting force of the raindrop (0.05-1.0 N (*71*)). The amount of water applied to the coating is equivalent to approximately 69,000 years of total annual rainfall in the Maryland area (40–50 inches per year (*72*)).

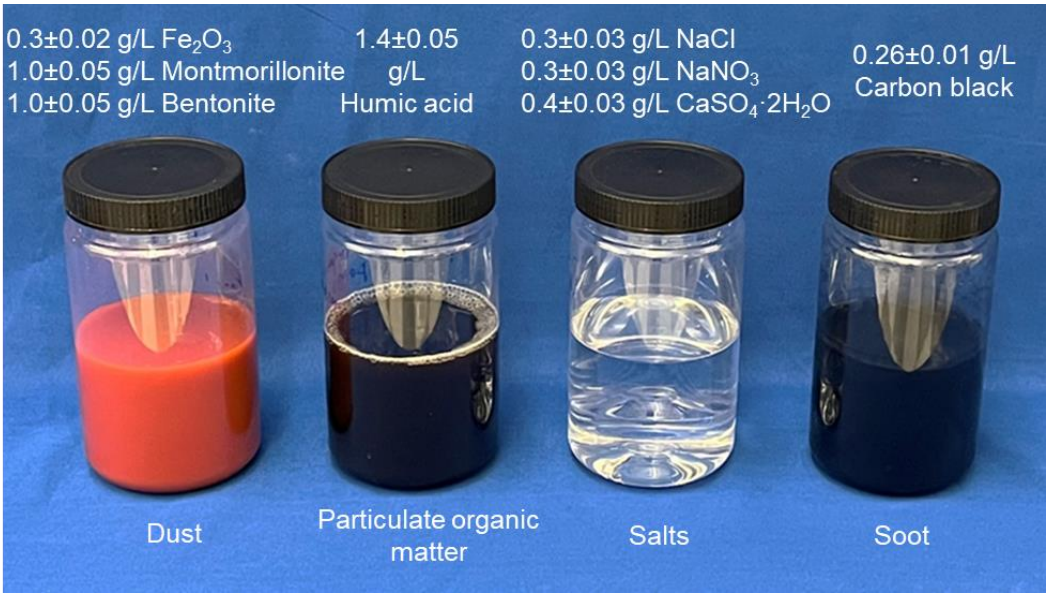

Figure S41. The soiling agents prepared for the laboratory soiling test, which follows ASMT D7897-18.

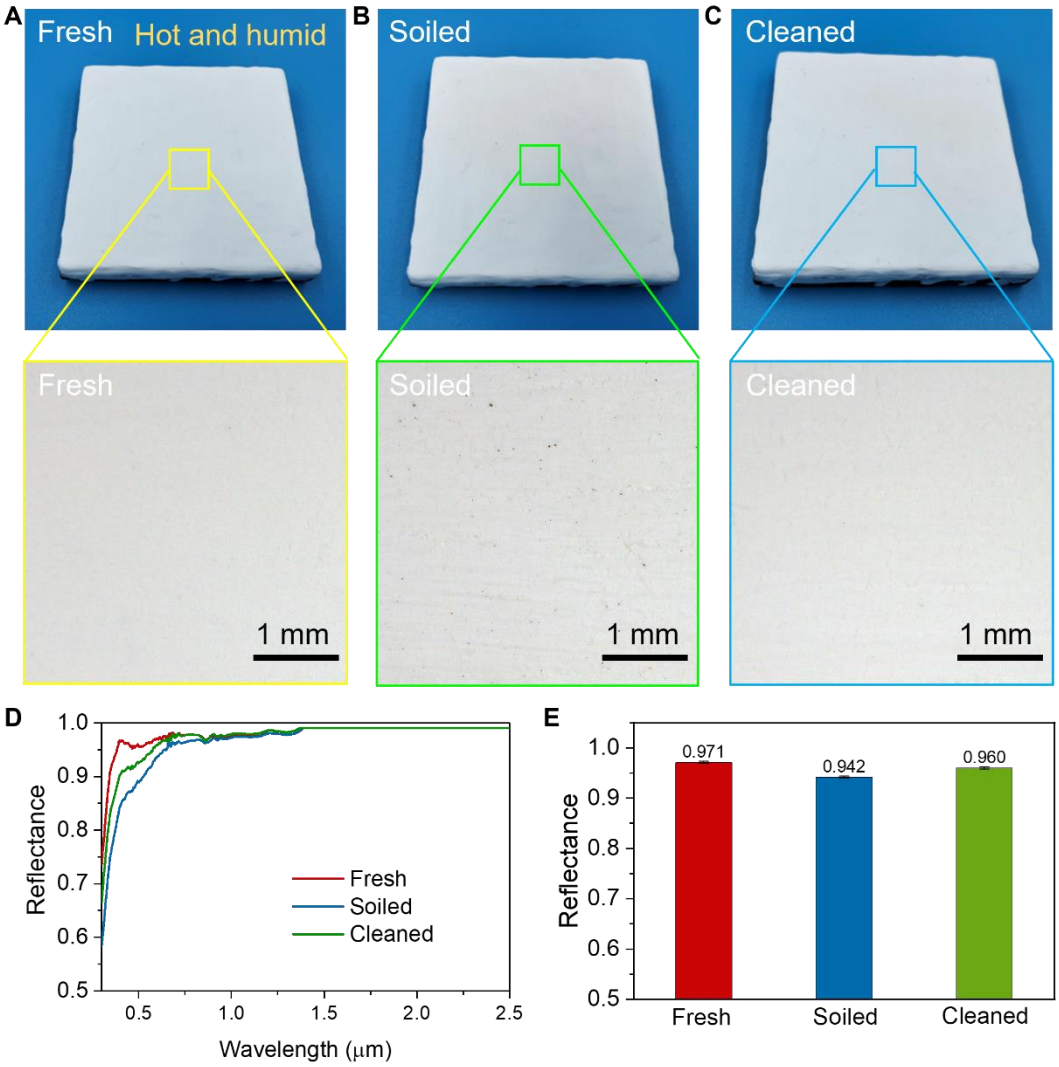

Figure S42. Laboratory soiling test simulating the hot and humid climate. Comparison of the appearance of the fresh (**A**), soiled (**B**), and cleaned (**C**) samples. (**D**) Comparison of the solar reflectance spectra of the fresh, soiled, and cleaned radiative cooling glass coating. (**E**) Comparison of the averaged solar reflectance of the fresh, soiled, and cleaned radiative cooling glass coating. The solar reflectance of the soiled radiative cooling glass coating decreased by about 3% due to the soiling agent consisting mainly of ~80 wt.% black POM and carbon soot. After blowing the soiled sample clean with air, the solar reflectance of the coating recovered to 0.96.

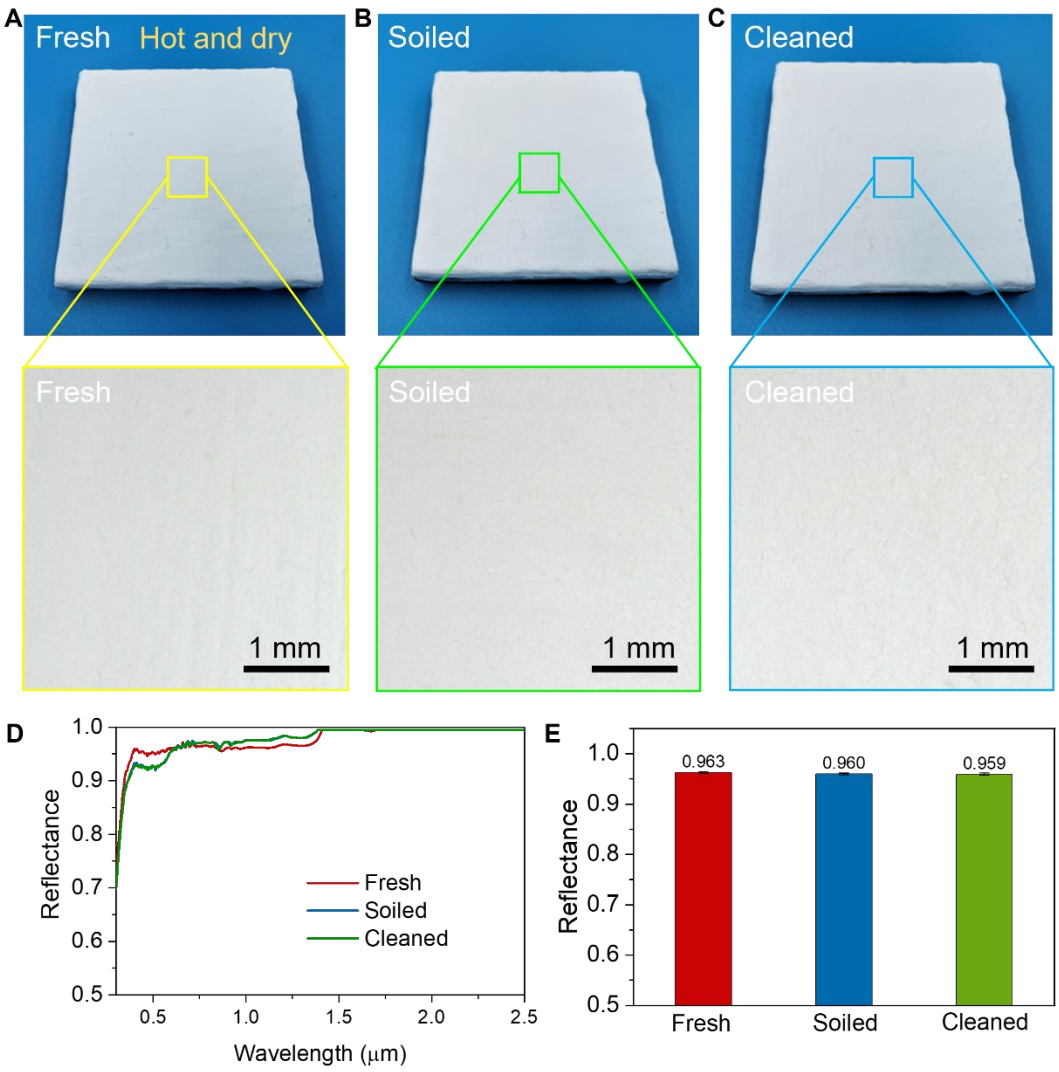

Figure S43. Laboratory soiling test simulating the hot and dry climate. Comparison of the appearance of the fresh (**A**), soiled (**B**), and cleaned (**C**) samples. (**D**) Comparison of the solar reflectance spectra of the fresh, soiled, and cleaned radiative cooling glass coating. (**E**) Comparison of the averaged solar reflectance of the fresh, soiled, and cleaned radiative cooling glass coating. Since the soiling agent consists mainly of dust and salt and does not contain black POM or carbon soot, we only saw a less than 1% decrease in solar reflectance after soiling. Cleaning with blowing air does not help to restore the solar reflectance of the radiative cooling glass coating because the dusty particles may enter the porous structures.

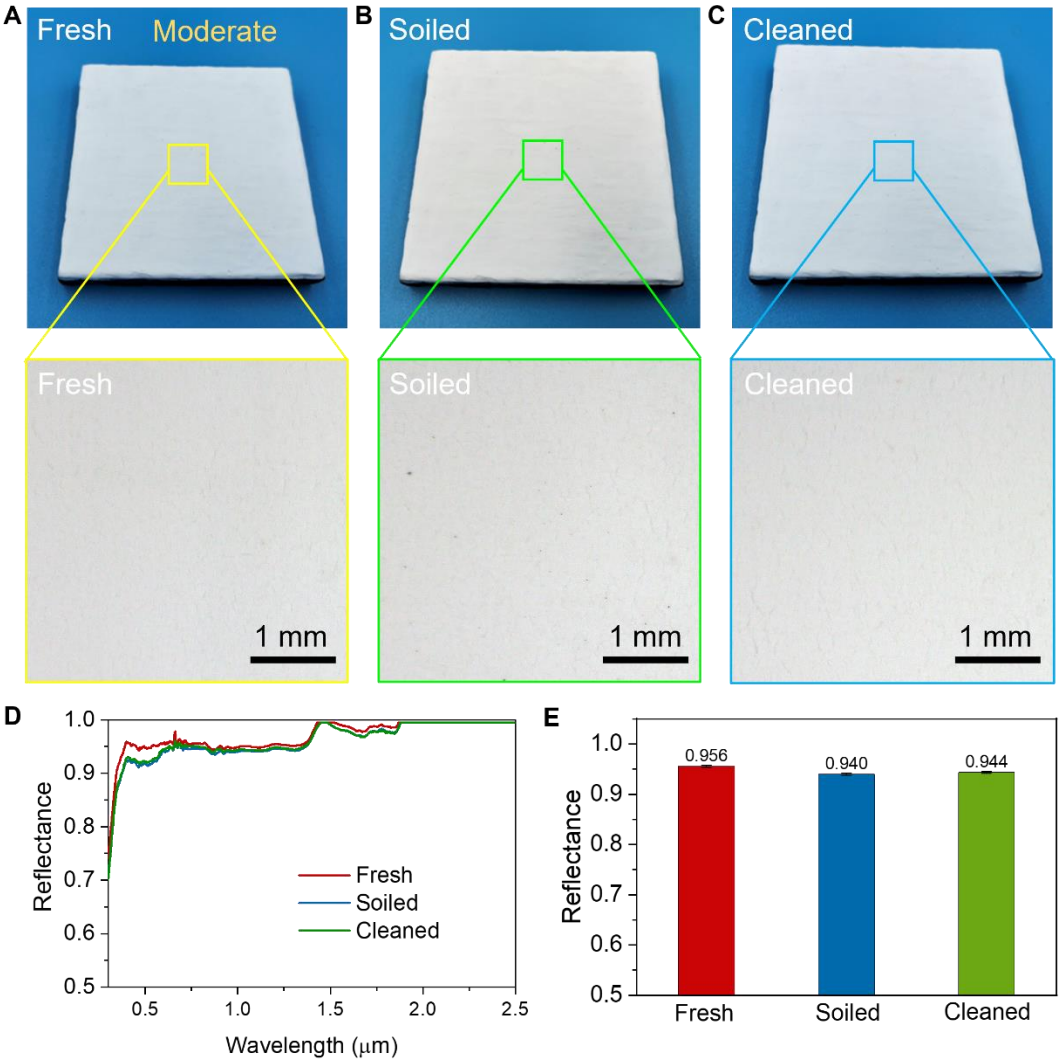

Figure S44. Laboratory soiling test simulating the moderate climate. Comparison of the appearance of the fresh (**A**), soiled (**B**), and cleaned (**C**) samples. (**D**) Comparison of the solar reflectance spectra of the fresh, soiled, and cleaned radiative cooling glass coating. (**E**) Comparison of the averaged solar reflectance of the fresh, soiled, and cleaned radiative cooling glass coating. The solar reflectance of the dirty radiative cooling glass coating decreases by ~1.6% due to the soiling agent consisting mainly of about 60 wt.% dust and 8 wt.% carbon soot. After cleaning with blowing air, the solar reflectance of the soiled coating can be improved by about 0.04% due to the removal of the carbon soot, which is about 1% lower than the reflectance of the new coating.

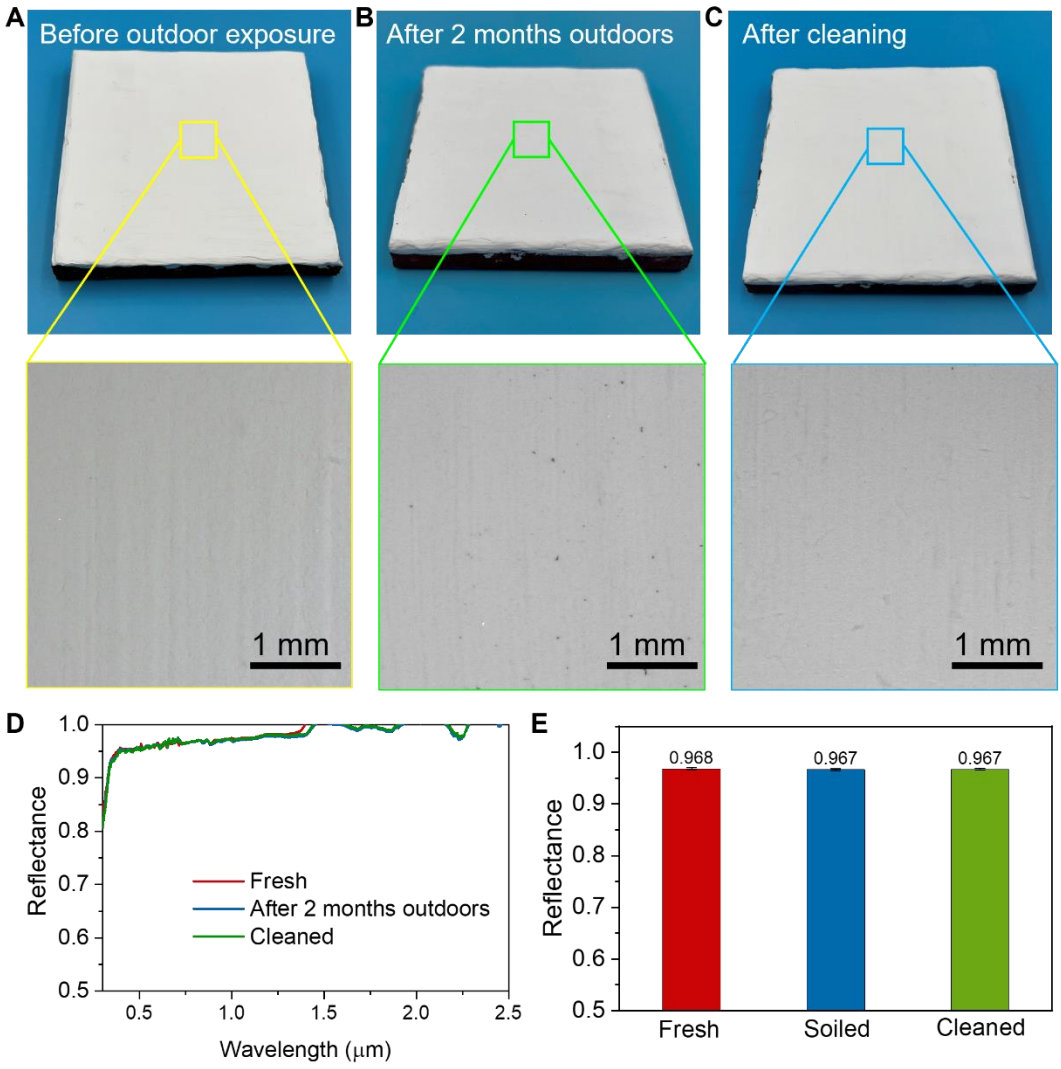

Figure S45. Comparative analysis of the radiative cooling glass coating: (**A**) freshly prepared, (**B**) after 2 months of outdoor exposure, and (**C**) post-cleaning. (**D**) Comparison of the spectral solar reflectance of the fresh, post-outdoor exposure, and cleaned radiative cooling glass coating. (**E**) Comparative analysis of the averaged solar reflectance for the fresh, after 2 months of outdoor exposure, and cleaned radiative cooling glass coating. The solar reflectance of the radiative cooling glass coating remains nearly constant after 2 months of outdoor exposure. We attribute the observed black particles on the coating surface to wildfires in Canada (*73*).

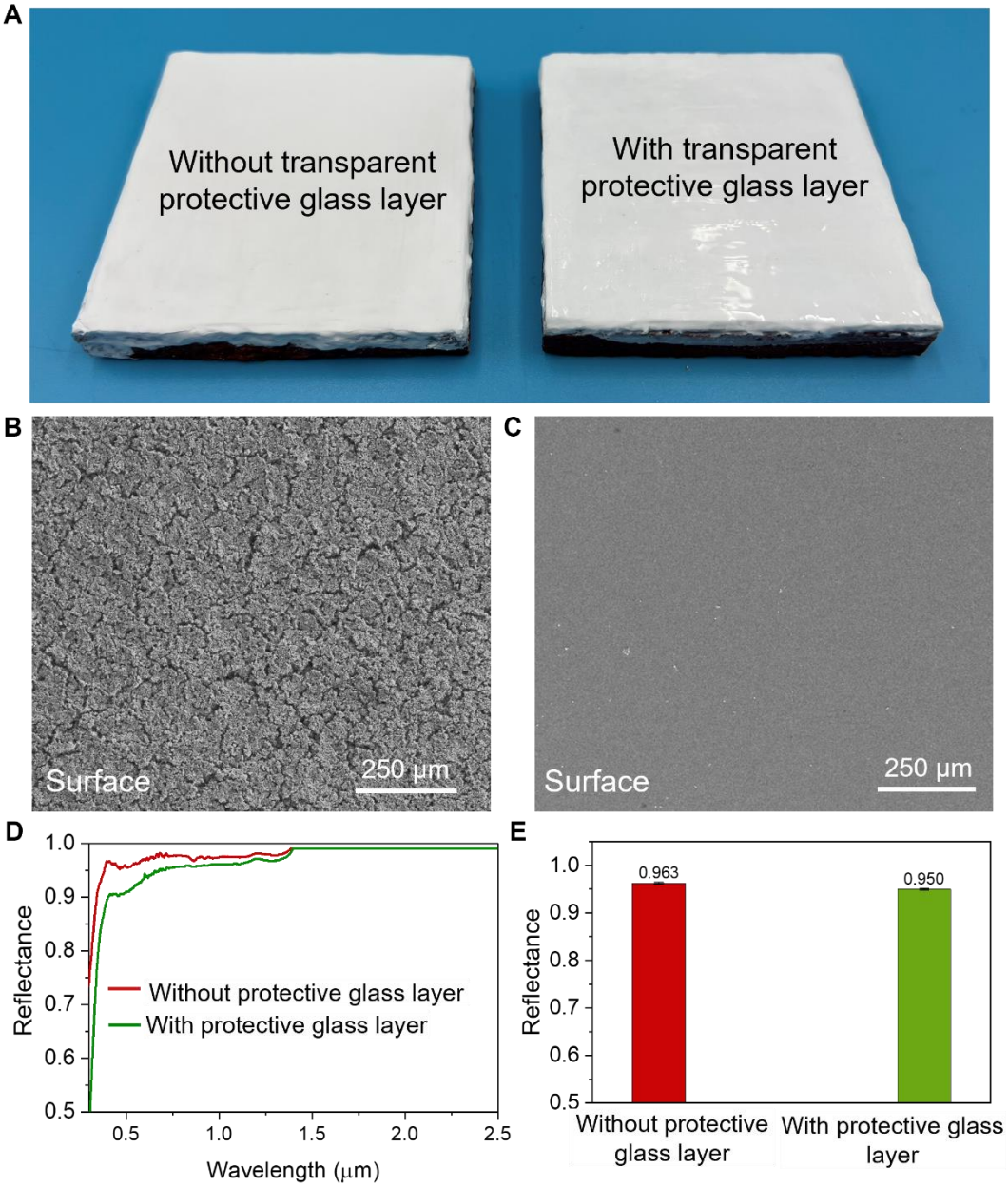

Figure S46. Comparison of the original radiative cooling glass coating with the radiative cooling glass coating covered with transparent protective glass. (**A**) Comparison of the appearance of the original radiative cooling glass coating (left) with the radiative cooling glass coating covered with the transparent protective glass layer (right). SEM images of (**B**) the original radiative cooling glass coating, and (**C**) the radiative cooling glass coating covered with the transparent protective glass layer. (**D**) Comparison of the solar reflectance spectra, and (**E**) averaged solar reflectance of the radiative cooling glass coating before and after the addition of the transparent protective glass layer. By adding the transparent dense glass coating with a thickness of ~10 μm, the averaged solar reflectance of the radiative cooling glass coating is reduced by ~1.3%, though still reaching ~0.95, which is close to most state-of-the-art daytime radiative cooling structures.

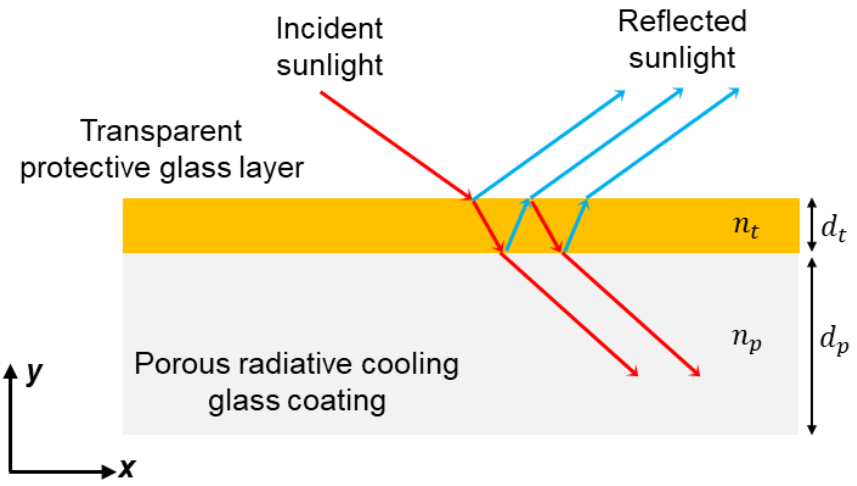

Figure S47. Schematic illustration of sunlight (unpolarized) transport across a radiative glass coating with a transparent protective glass layer.

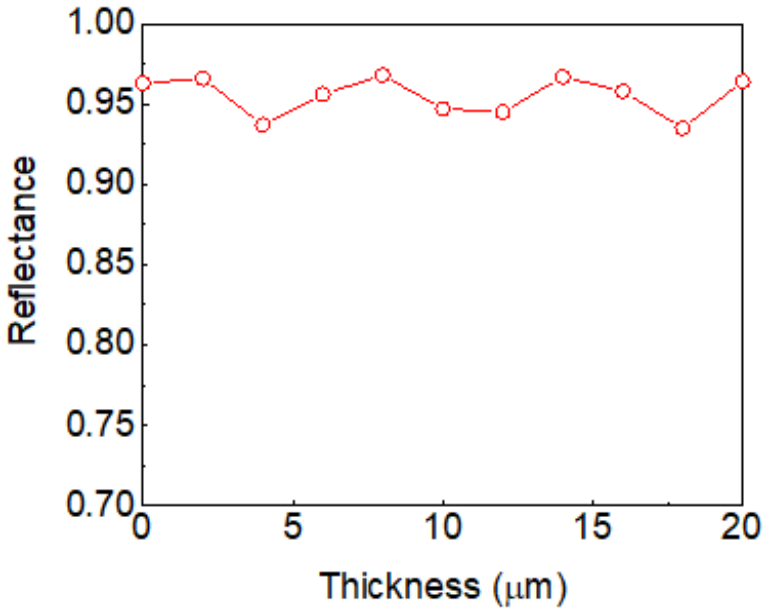

Figure S48. Dependence of the reflectance of the radiative cooling glass coating (0.5 μm thick) on the thickness of the transparent protective glass layer, simulated at a wavelength of 500 nm. Due to interference patterns between light reflections from different interfaces, the reflectance of the overall structure alternates between peaks and troughs, ranging from 0.935 to 0.968 (within a 3% margin), with an average of 0.954, in correlation with the increase in protective glass layer's thickness.

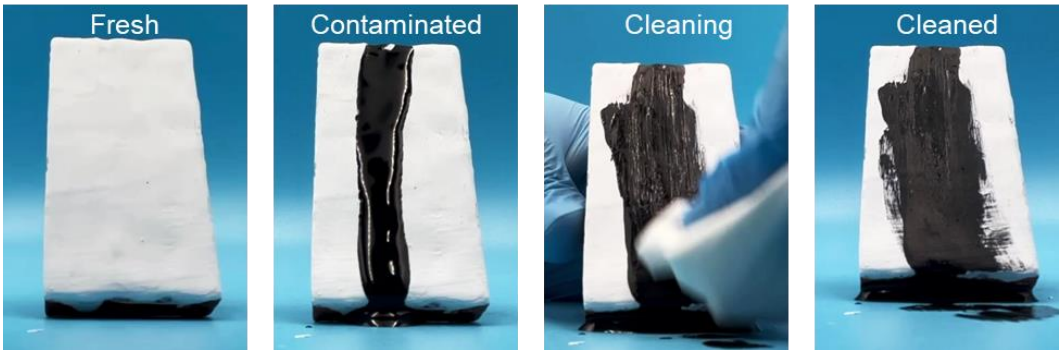

Figure S49. Photographs of the liquid pollutant (high concentration carbon nanoparticles dispersed in water to demonstrate an extreme soiling condition) applied to the radiative cooling glass coating. Due to the microporous structure, the liquid pollutant permeates the cooling glass coating, markedly reducing the solar reflectance.

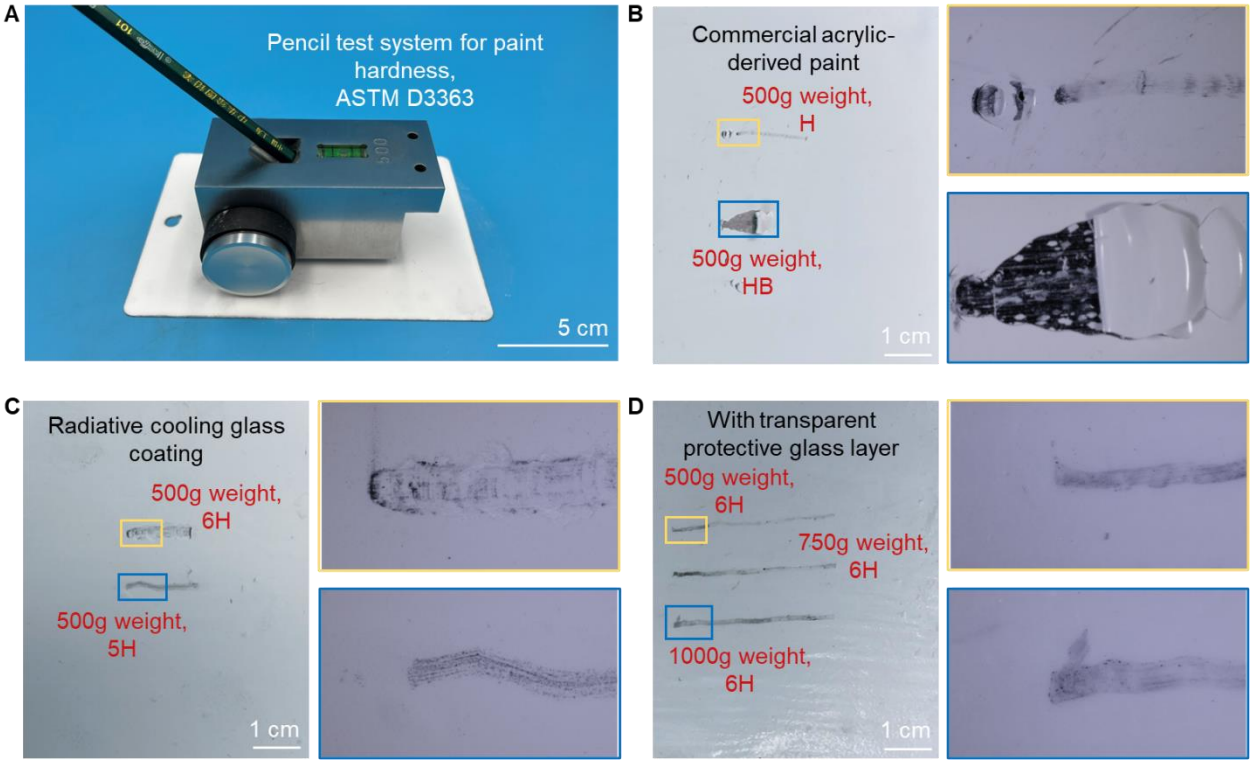

Figure S50. Evaluation of the surface hardness of the coatings. (**A**) The pencil test system for paint hardness, following ASTM D3363-22 (*53*). (**B**) Photographs illustrating the test results of commercial acrylic-derived paints, displaying a hardness of 'H' under a weight of 500 g. (**C**) Photographs showing the test results of the radiative cooling glass coating, demonstrating a hardness of '5H' under a weight of 500 g. (**D**) Photographs presenting the test results of the radiative cooling glass coating with a protective glass layer. No scratches were observed on the surface when a '6H' pencil was used, even when the applied weight reached 1000 g.

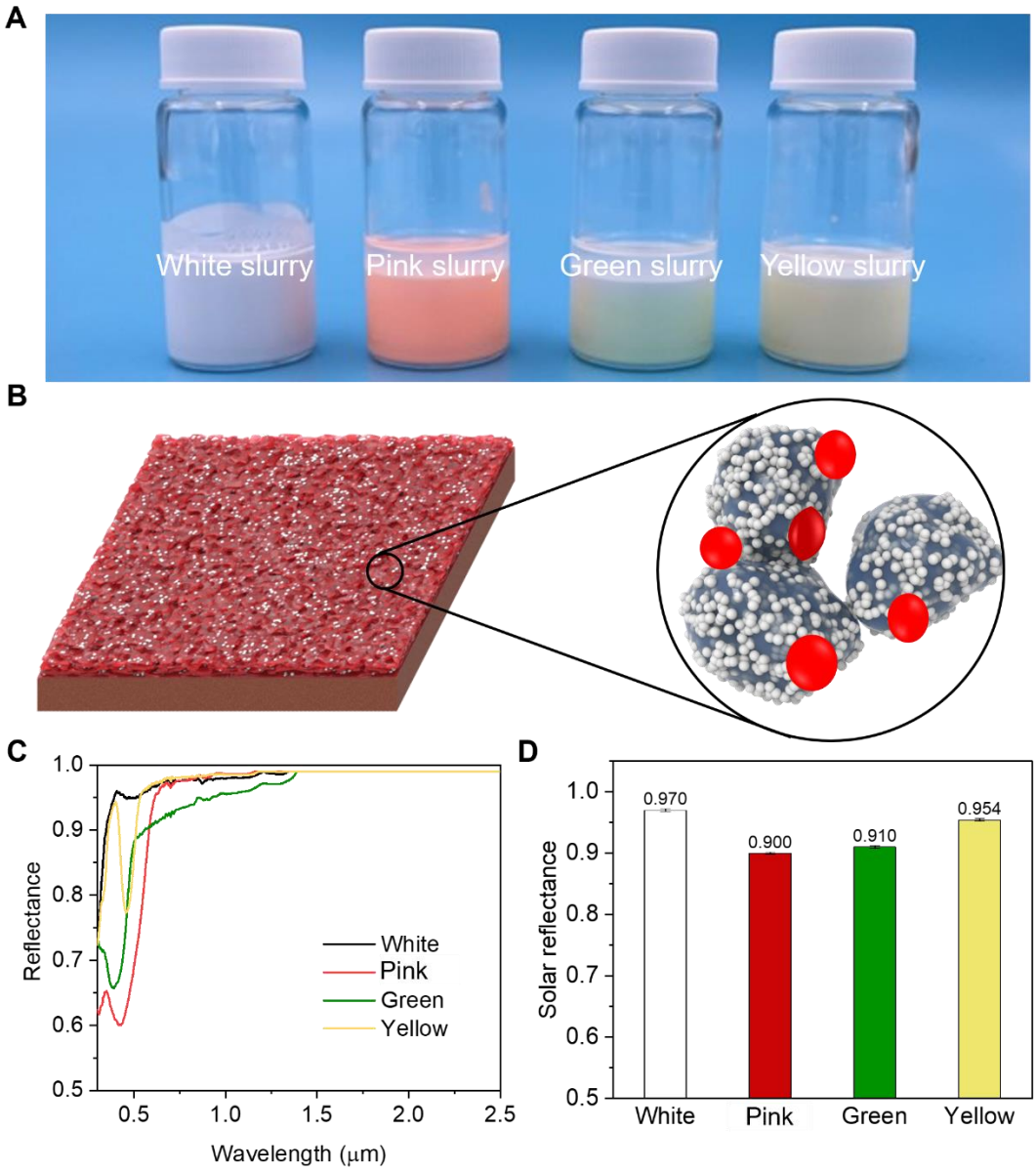

Figure S51. Manufacturing and optical characterization of the colored radiative cooling structures. (**A**) Photograph of the white (50 wt.% Al_2O_3 and 50 wt.% glass), pink (45 wt.% Al_2O_3, 45 wt.% glass, and 10 wt.% Nitride($CaAlSiN_3:Eu^{2+}$)), green (45 wt.% Al_2O_3, 45 wt.% glass, and 10 wt.% $(Sr,Ba)_2SiO_4:Eu^{2}$), and yellow (45 wt.% Al_2O_3, 45 wt.% glass, and 10 wt.% (Ce,Gd):YAG) slurries for fabricating the white and colored radiative cooling structures. (**B**) Schematic of the colored radiative cooling glass coating, which is fabricated by adding dyes to the mixture of the glass microparticles and Al_2O_3 particles. (**C**) Comparison of the solar reflectance of the white and colored radiative cooling glass coatings in the solar spectrum. (**D**) Comparison of the averaged solar reflectance of the white and colored radiative cooling glass coatings.

References and Notes

1. United Nations Environment Programme (UNEP) and International Energy Agency (IEA), *Cooling Emissions and Policy Synthesis Report: Benefits of cooling efficiency and the Kigali Amendment* (UNEP and IEA, 2020).

2. J. Woods, N. James, E. Kozubal, E. Bonnema, K. Brief, L. Voeller, J. Rivest, Humidity's impact on greenhouse gas emissions from air conditioning. *Joule* **6**, 726–741 (2022). doi:10.1016/j.joule.2022.02.013

3. International Energy Agency (IEA), *The Future of Cooling: Opportunities for Energy Efficient Air Conditioning* (IEA, 2018); https://doi.org/10.1787/9789264301993-en.

4. X. Yin, R. Yang, G. Tan, S. Fan, Terrestrial radiative cooling: Using the cold universe as a renewable and sustainable energy source. *Science* **370**, 786–791 (2020). doi:10.1126/science.abb0971 Medline

5. D. Zhao, A. Aili, Y. Zhai, S. Xu, G. Tan, X. Yin, R. Yang, Radiative sky cooling: Fundamental principles, materials, and applications. *Appl. Phys. Rev.* **6**, 021306 (2019). doi:10.1063/1.5087281

6. E. Teitelbaum, K. W. Chen, D. Aviv, K. Bradford, L. Ruefenacht, D. Sheppard, M. Teitelbaum, F. Meggers, J. Pantelic, A. Rysanek, Membrane-assisted radiant cooling for expanding thermal comfort zones globally without air conditioning. *Proc. Natl. Acad. Sci. U.S.A.* **117**, 21162–21169 (2020). doi:10.1073/pnas.2001678117 Medline

7. J. Kośny, D. W. Yarbrough, "Short history of thermal insulation and radiation control technologies used in architecture" in *Thermal Insulation and Radiation Control Technologies for Buildings*, J. Kośny, D. W. Yarbrough, Eds. (Springer, 2022), pp. 1–35.

8. L. Zhu, A. Raman, K. X. Wang, M. A. Anoma, S. Fan, Radiative cooling of solar cells. *Optica* **1**, 32–38 (2014). doi:10.1364/OPTICA.1.000032

9. A. Aili, D. Zhao, G. Tan, X. Yin, R. Yang, Reduction of water consumption in thermal power plants with radiative sky cooling. *Appl. Energy* **302**, 117515 (2021). doi:10.1016/j.apenergy.2021.117515

10. P.-C. Hsu, A. Y. Song, P. B. Catrysse, C. Liu, Y. Peng, J. Xie, S. Fan, Y. Cui, Radiative human body cooling by nanoporous polyethylene textile. *Science* **353**, 1019–1023 (2016). doi:10.1126/science.aaf5471 Medline

11. S. Zeng, S. Pian, M. Su, Z. Wang, M. Wu, X. Liu, M. Chen, Y. Xiang, J. Wu, M. Zhang, Q. Cen, Y. Tang, X. Zhou, Z. Huang, R. Wang, A. Tunuhe, X. Sun, Z. Xia, M. Tian, M. Chen, X. Ma, L. Yang, J. Zhou, H. Zhou, Q. Yang, X. Li, Y. Ma, G. Tao, Hierarchical-morphology metafabric for scalable passive daytime radiative cooling. *Science* **373**, 692–696 (2021). doi:10.1126/science.abi5484 Medline

12. M. Zhou, H. Song, X. Xu, A. Shahsafi, Y. Qu, Z. Xia, Z. Ma, M. A. Kats, J. Zhu, B. S. Ooi, Q. Gan, Z. Yu, Vapor condensation with daytime radiative cooling. *Proc. Natl. Acad. Sci. U.S.A.* **118**, e2019292118 (2021). doi:10.1073/pnas.2019292118 Medline

13. J. N. Munday, Tackling climate change through radiative cooling. *Joule* **3**, 2057–2060 (2019). doi:10.1016/j.joule.2019.07.010

14. J. Li, Y. Liang, W. Li, N. Xu, B. Zhu, Z. Wu, X. Wang, S. Fan, M. Wang, J. Zhu, Protecting ice from melting under sunlight via radiative cooling. *Sci. Adv.* **8**, eabj9756 (2022). doi:10.1126/sciadv.abj9756 Medline

15. A. P. Raman, M. A. Anoma, L. Zhu, E. Rephaeli, S. Fan, Passive radiative cooling below ambient air temperature under direct sunlight. *Nature* **515**, 540–544 (2014). doi:10.1038/nature13883 Medline

16. M. M. Hossain, B. Jia, M. Gu, A metamaterial emitter for highly efficient radiative cooling. *Adv. Opt. Mater.* **3**, 1047–1051 (2015). doi:10.1002/adom.201500119

17. D. Chae, M. Kim, P.-H. Jung, S. Son, J. Seo, Y. Liu, B. J. Lee, H. Lee, Spectrally selective inorganic-based multilayer emitter for daytime radiative cooling. *ACS Appl. Mater. Interfaces* **12**, 8073–8081 (2020). doi:10.1021/acsami.9b16742 Medline

18. K. Tang, K. Dong, J. Li, M. P. Gordon, F. G. Reichertz, H. Kim, Y. Rho, Q. Wang, C.-Y. Lin, C. P. Grigoropoulos, A. Javey, J. J. Urban, J. Yao, R. Levinson, J. Wu, Temperature-adaptive radiative coating for all-season household thermal regulation. *Science* **374**, 1504–1509 (2021). doi:10.1126/science.abf7136 Medline

19. Y. Zhai, Y. Ma, S. N. David, D. Zhao, R. Lou, G. Tan, R. Yang, X. Yin, Scalable-manufactured randomized glass-polymer hybrid metamaterial for daytime radiative cooling. *Science* **355**, 1062–1066 (2017). doi:10.1126/science.aai7899 Medline

20. L. Zhou, H. Song, J. Liang, M. Singer, M. Zhou, E. Stegenburgs, N. Zhang, C. Xu, T. Ng, Z. Yu, B. Ooi, Q. Gan, A polydimethylsiloxane-coated metal structure for all-day radiative cooling. *Nat. Sustain.* **2**, 718–724 (2019). doi:10.1038/s41893-019-0348-5

21. J. Mandal, Y. Fu, A. C. Overvig, M. Jia, K. Sun, N. N. Shi, H. Zhou, X. Xiao, N. Yu, Y. Yang, Hierarchically porous polymer coatings for highly efficient passive daytime radiative cooling. *Science* **362**, 315–319 (2018). doi:10.1126/science.aat9513 Medline

22. A. Leroy, B. Bhatia, C. C. Kelsall, A. Castillejo-Cuberos, M. Di Capua H, L. Zhao, L. Zhang, A. M. Guzman, E. N. Wang, High-performance subambient radiative cooling enabled by optically selective and thermally insulating polyethylene aerogel. *Sci. Adv.* **5**, eaat9480 (2019). doi:10.1126/sciadv.aat9480 Medline

23. J. Mandal, Y. Yang, N. Yu, A. P. Raman, Paints as a scalable and effective radiative cooling technology for buildings. *Joule* **4**, 1350–1356 (2020). doi:10.1016/j.joule.2020.04.010

24. X. Li, J. Peoples, Z. Huang, Z. Zhao, J. Qiu, X. Ruan, Full daytime sub-ambient radiative cooling in commercial-like paints with high figure of merit. *Cell Rep. Phys. Sci.* **1**, 100221 (2020). doi:10.1016/j.xcrp.2020.100221

25. X. Li, J. Peoples, P. Yao, X. Ruan, Ultrawhite $BaSO_4$ paints and films for remarkable daytime subambient radiative cooling. *ACS Appl. Mater. Interfaces* **13**, 21733–21739 (2021). doi:10.1021/acsami.1c02368 Medline

26. T. Li, Y. Zhai, S. He, W. Gan, Z. Wei, M. Heidarinejad, D. Dalgo, R. Mi, X. Zhao, J. Song, J. Dai, C. Chen, A. Aili, A. Vellore, A. Martini, R. Yang, J. Srebric, X. Yin, L. Hu, A radiative cooling structural material. *Science* **364**, 760–763 (2019). doi:10.1126/science.aau9101 Medline

27. S. Wang, T. Jiang, Y. Meng, R. Yang, G. Tan, Y. Long, Scalable thermochromic smart windows with passive radiative cooling regulation. *Science* **374**, 1501–1504 (2021). doi:10.1126/science.abg0291 Medline

28. H. Takebayashi, K. Miki, K. Sakai, Y. Murata, T. Matsumoto, S. Wada, T. Aoyama, Experimental examination of solar reflectance of high-reflectance paint in Japan with natural and accelerated aging. *Energy Build.* **114**, 173–179 (2016). doi:10.1016/j.enbuild.2015.06.019

29. C. Lin, Y. Li, C. Chi, Y. S. Kwon, J. Huang, Z. Wu, J. Zheng, G. Liu, C. Y. Tso, C. Y. H. Chao, B. Huang, A solution-processed inorganic emitter with high spectral selectivity for efficient subambient radiative cooling in hot humid climates. *Adv. Mater.* **34**, e2109350 (2022). doi:10.1002/adma.202109350 Medline

30. H.-Y. Wu, S.-R. Huang, C.-H. Shih, L.-J. Hsiao, H.-W. Chen, M.-C. Cheng, J.-C. Hsu, Highly reflective silver-enhanced coating with high adhesion and sulfurization resistance for telescopes. *Nanomaterials* **12**, 1054 (2022). doi:10.3390/nano12071054 Medline

31. A. García-Segura, A. Fernández-García, M. Ariza, F. Sutter, L. Valenzuela, Durability studies of solar reflectors: A review. *Renew. Sustain. Energy Rev.* **62**, 453–467 (2016). doi:10.1016/j.rser.2016.04.060

32. R. Bethea, M. Barriger, P. Williams, S. Chin, Environmental effects on solar concentrator mirrors. *Sol. Energy* **27**, 497–511 (1981). doi:10.1016/0038-092X(81)90045-1

33. H. Bao, C. Yan, B. Wang, X. Fang, C. Y. Zhao, X. Ruan, Double-layer nanoparticle-based coatings for efficient terrestrial radiative cooling. *Sol. Energy Mater. Sol. Cells* **168**, 78–84 (2017). doi:10.1016/j.solmat.2017.04.020

34. A. R. Gentle, G. B. Smith, Radiative heat pumping from the Earth using surface phonon resonant nanoparticles. *Nano Lett.* **10**, 373–379 (2010). doi:10.1021/nl903271d Medline

35. S. Atiganyanun, J. B. Plumley, S. J. Han, K. Hsu, J. Cytrynbaum, T. L. Peng, S. M. Han, S. E. Han, Effective radiative cooling by paint-format microsphere-based photonic random media. *ACS Photonics* **5**, 1181–1187 (2018). doi:10.1021/acsphotonics.7b01492

36. T. Li, H. Sun, M. Yang, C. Zhang, S. Lv, B. Li, L. Chen, D. Sun, All-ceramic, compressible and scalable nanofibrous aerogels for subambient daytime radiative cooling. *Chem. Eng. J.* **452**, 139518 (2023). doi:10.1016/j.cej.2022.139518

37. T. G. Hawarden, R. Crane, H. A. Thronson, A. J. Penny, A. H. Orlowska, T. W. Bradshaw, "Radiative and hybrid cooling of infrared space telescopes" in *Infrared and Submillimeter Space Missions in the Coming Decade*, H. A. Thronson, M. Sauvage, P. Gallais, L. Vigroux, Eds. (Springer Dordrecht, 1995), pp. 45–56.

38. M. Holynska, Y. Butenko, R. Martins, C. Semprimoschnig, F. Meyer, S. Faber, Studies of white ceramic coatings for ESA's BepiColombo mission to Mercury. *J. Spacecr. Rockets* **56**, 1358–1370 (2019). doi:10.2514/1.A34230

39. H. Masai, T. Nishibe, S. Yamamoto, T. Niizuma, N. Kitamura, T. Akai, T. Ohkubo, M. Yoshida, Low melting oxide glasses prepared at a melt temperature of 500 °C. *Sci. Rep.* **11**, 214 (2021). doi:10.1038/s41598-020-80424-9 Medline

40. W. Jin, P. K. Chu, "Orthopedic implants" in *Encyclopedia of Biomedical Engineering: Volume 2*, R. Narayan, Ed. (Elsevier, 2019), pp. 425–439.

41. See supplementary materials.

42. Flexcompute, Tidy3D: Next-gen Electromagnetic Simulation Tool, Example Library: Nanophotonics—Radiative cooling glass coating; https://www.flexcompute.com/tidy3d/examples/notebooks/RadiativeCoolingGlass/.

43. M. P. Diebold, *Application of Light Scattering to Coatings: A User's Guide* (Springer, 2014).

44. M. C. Baechler, J. L. Williamson, T. L. Gilbride, P. C. Cole, M. G. Hefty, P. M. Love, "Building America best practices series: volume 7.1: Guide to determining climate regions by county" (Pacific Northwest National Lab, 2010); https://doi.org/10.2172/1068658.

45. H. Zhong, P. Zhang, Y. Li, X. Yang, Y. Zhao, Z. Wang, Highly solar-reflective structures for daytime radiative cooling under high humidity. *ACS Appl. Mater. Interfaces* **12**, 51409–51417 (2020). doi:10.1021/acsami.0c14075 Medline

46. EnergyPlus software; https://energyplus.net/.

47. P. C. Tabares-Velasco, C. Christensen, M. Bianchi, Verification and validation of EnergyPlus phase change material model for opaque wall assemblies. *Build. Environ.* **54**, 186–196 (2012). doi:10.1016/j.buildenv.2012.02.019

48. ASTM Standard D3359-22, "Standard Test Methods for Rating Adhesion by Tape Test" (ASTM International, 2023); https://doi.org/10.1520/D3359-22.

49. M. M. Shokrieh, A. Bayat, Effects of ultraviolet radiation on mechanical properties of glass/polyester composites. *J. Compos. Mater.* **41**, 2443–2455 (2007). doi:10.1177/0021998307075441

50. L. Jacques, Accelerated and outdoor/natural exposure testing of coatings. *Prog. Polym. Sci.* **25**, 1337–1362 (2000). doi:10.1016/S0079-6700(00)00030-7

51. ASTM Standard D7897-18, "Standard Practice for Laboratory Soiling and Weathering of Roofing Materials to Simulate Effects of Natural Exposure on Solar Reflectance and Thermal Emittance" (ASTM International, 2018); https://doi.org/10.1520/D7897-18.

52. ASTM Standard D3359-17, "Standard Test Methods for Rating Adhesion by Tape Test" (ASTM International, 2017); https://doi.org/10.1520/D3359-17.

53. ASTM Standard D3363-22, "Standard Test Method for Film Hardness by Pencil Test" (ASTM International, 2022); https://doi.org/10.1520/D3363-22.

54. M.-T. Tsai, S.-W. Chang, Y.-J. Chen, H.-L. Chen, P.-H. Lan, D. Chen, F.-H. Ko, Y.-C. Lo, H.-C. Wang, D. Wan, Scalable, flame-resistant, superhydrophobic ceramic metafibers for sustainable all-day radiative cooling. *Nano Today* **48**, 101745 (2023). doi:10.1016/j.nantod.2022.101745

55. C. Mätzler, "MATLAB functions for Mie scattering and absorption," Institute of Applied Physics (IAP), University of Bern, Research Report No. 2002-08 (2002).

56. X. Zhao, S. A. Mofid, B. P. Jelle, G. Tan, X. Yin, R. Yang, Optically-switchable thermally-insulating VO_2-aerogel hybrid film for window retrofits. *Appl. Energy* **278**, 115663 (2020). doi:10.1016/j.apenergy.2020.115663

57. A. Aili, X. Yin, R. Yang, Passive sub-ambient cooling: Radiative cooling versus evaporative cooling. *Appl. Therm. Eng.* **202**, 117909 (2022). doi:10.1016/j.applthermaleng.2021.117909

58. D. Zhao, A. Aili, Y. Zhai, J. Lu, D. Kidd, G. Tan, X. Yin, R. Yang, Subambient cooling of water: Toward real-world applications of daytime radiative cooling. *Joule* **3**, 111–123 (2019). doi:10.1016/j.joule.2018.10.006

59. Spectral Sciences Inc., MODTRAN (MODerate resolution atmospheric TRANsmission); http://modtran.spectral.com/.

60. US Energy Information Administration, State Electricity Profiles (2022); https://www.eia.gov/electricity/state/.

61. US Energy Information Administration, Natural Gas Annual (2022); https://www.eia.gov/naturalgas/annual/.

62. US Environmental Protection Agency, "AP-42: Compilation of air pollutant emission factors, fifth edition" (1995); https://www.epa.gov/air-emissions-factors-and-quantification/ap-42-compilation-air-emissions-factors.

63. US Energy Information Administration, "Updated state-level greenhouse gas emission coefficients for electricity generation 1998-2000" (2002).

64. M. Deru, K. Field, D. Studer, K. Benne, B. Griffith, P. Torcellini, B. Liu, M. Halverson, D. Winiarski, M. Rosenberg, M. Yazdanian, J. Huang, D. Crawley, "US Department of Energy commercial reference building models of the national building stock," Tech. Rep. NREL/TP-5500-46861 (National Renewable Energy Laboratory, 2011).

65. S. Goel, R. A. Athalye, W. Wang, J. Zhang, M. I. Rosenberg, Y. Xie, P. R. Hart, V. V. Mendon, "Enhancements to ASHRAE standard 90.1 prototype building models," Tech. Rep. PNNL-23269 (Pacific Northwest National Laboratory, 2014); https://doi.org/10.2172/1129366.

66. M. N. Polyanskiy, RefractiveIndex.INFO–Refractive index database, Optical constants of SCHOTT - PK (Phosphate crown); https://refractiveindex.info/?shelf=glass&book=SCHOTT-PK&page=N-PK51.

67. M. N. Polyanskiy, RefractiveIndex.INFO–Refractive index database, Optical constants of Al_2O_3 (Aluminium sesquioxide, Sapphire, Alumina); https://refractiveindex.info/?shelf=main&book=Al2O3&page=Querry-o.

68. M. N. Polyanskiy, RefractiveIndex.INFO–Refractive index database, Optical constants of SiO_2 (Silicon dioxide, Silica, Quartz); https://refractiveindex.info/?shelf=main&book=SiO2&page=Popova.

69. Q. Fu, "Cloud-radiative processes" in *Encyclopedia of Atmospheric Sciences: Volume 5*, G. R. North, J. A. Pyle, F. Zhang, Eds. (Academic Press, ed. 2, 2015), pp. 13–15.

70. A. Papyrin, V. Kosarev, S. Klinkov, A. Alkhimov, V. M. Fomin, *Cold Spray Technology* (Elsevier, 2006).

71. D. Soto, A. B. De Larivière, X. Boutillon, C. Clanet, D. Quéré, The force of impacting rain. *Soft Matter* **10**, 4929–4934 (2014). doi:10.1039/C4SM00513A Medline

72. J. Runkle, K. E. Kunkel, D. R. Easterling, B. C. Stewart, S. M. Champion, R. Frankson, W. Sweet, J. Spaccio, Maryland and the District of Columbia State Climate Summary 2022, NOAA Technical Report NESDIS 150-MD (NOAA/NESDIS, 2022); https://statesummaries.ncics.org/chapter/md/#:~:text=Annual%20average%20precipitation%20in%20Maryland,eastern%20areas%20of%20the%20state.

73. M. Berg, "D.C. issues Code Red air quality due to Canada wildfires," Politico, 29 June 2023; https://www.politico.com/news/2023/06/29/air-quality-washington-alert-00104161.